Improvement of modified maximum force criterion for forming limit diagram prediction of sheet metal

Quoc Tuan Pham [a],[*], Md Shafiqul Islam [a], Mats Sigvant [a],[b], Lluís Pérez Caro [c], Myoung-Gyu Lee [d], Young-Suk Kim [e]

[a] Department of Mechanical Engineering, Blekinge Institute of Technology, Karlskrona, Sweden
[b] Volvo Cars, Department 81110 Strategy Development, Olofström, Sweden
[c] RISE Research Institutes of Sweden, Component Manufacturing Unit, Olofström, Sweden
[d] Department of Materials Science and Engineering & RIAM, Seoul National University, Seoul 08826, Republic of Korea
[e] School of Mechanical Engineering, Kyungpook National University, Daegu 41566, Republic of Korea

ARTICLE INFO

ABSTRACT

This study presents a new criterion (MMFC2) for predicting the forming limit curve (FLC) of sheet metal. The strain path evolution of a critical element examined in a uniaxial tensile test is elaborated by incorporating the results of experimental measurement, finite element simulation, and theoretical prediction via the Modified Maximum Force Criterion (MMFC). A scaling factor is introduced to mimic the theoretical evaluation with the simulated one. It is believed that the rotation of the principal axes of the theoretically considering material point, which is initially co-axial with the external load coordinate, implicates the macro track of the strain path change. Furthermore, an optimal event of the second derivative of the axial rotations is proposed to indicate the strain localization and formulate the FLC. The performance of the proposed criterion is compared with that of the original MMFC in predicting the FLC of three automotive sheet metals, of which all related data were published in the Benchmark of Numisheet 2014 conference. The use of three different hardening laws and three yield functions is examined in the analogy. The comparison reveals that the results of MMFC2 are more sensitive to the employed constitutive model than that of MMFC. Furthermore, the proposed MMFC2 presents concordant results with the experimental data. Nakajima tests are conducted for CR4 mild steel sheets to validate the capacity of the proposed criterion. Well agreement between the experimentally measured data and theoretical prediction based on the Yld2k yield function verifies its usefulness in practice.

1. Introduction

In the vast majority of sheet metal forming, evaluation of the material's formability is essential for designing new parts and testing formed products. For this purpose, the forming limit diagram (FLD) has been widely accepted in the community. This method establishes a forming limit curve (FLC) to graphically indicate the material's localization in various strain paths, ranging from uniaxial to equi-biaxial tension. For decades, standard testing methods such as Nakajima tests and Marciniak tests (Marciniak and Kuczyński, 1967) have been constructed to provide guidance for obtaining experimentally reliable FLC. However, high costs, involved uncertainties, and shortages are the main disadvantages of these experimental methods. Therefore, numerous methods have been proposed to predict the FLC of sheet metal theoretically.

In the same year, Swift (1952) and Hill (1952) proposed pioneering criteria for necking initiation. The former assumed that the necking

phenomenon occurs when the loading force gains its maximum. In the latter one, the necking occurrence is stated at the instance of maximum force per unit width in the major direction. Nowadays, the phenomenon indicated due to Swift (1952) is known as the diffuse neck, whereas the phenomenon observed due to Hill (1952) is known as the localized neck. Because of their theoretical assumptions, Swift's model can predict the entire range of FLC, but Hill's criterion is only available for the left side. However, the prediction of Hill's model is agreed with experimental measurements of various materials better than that of Swift's. Therefore, several studies combined the predictions of Hill's and Swift's models for the left and right parts of FLC prediction (Bleck et al., 1998; Djavanroodi and Derogar, 2010; Ganjiani and Assempour, 2007).

Based on an assumption of material's imperfection, Marciniak and Kuczynski proposed a numerical method well-known as the MK model

---

* Corresponding author.
  E-mail address: quoc.tuan.pham@bth.se (Q.T. Pham).

(Marciniak and Kuczyński, 1967) for predicting the right side of FLC. The model was extended to the left-side of FLC by Hutchinson and Neale (1978). Nowadays, this model is the most widely used for the theoretical prediction of sheet metal's FLC. In the literature, the performance of this model has been examined with various constitutive equations (Kuroda and Tvergaard, 2000; Butuc et al., 2002; Yoshida et al., 2007), polycrystalline models (Butuc et al., 2021; Zhang et al., 2014; Schwindt et al., 2015), as well as damage models (Kim et al., 2003; Son and Kim, 2003). The MK model has been further extended to consider the effect of material parameters (Mohammadi et al., 2014), process parameters (Aretz, 2007; Chu et al., 2014), and three-dimensional stress states (Eyckens et al., 2009; Allwood and Shouler, 2009). An interesting and comprehensive review of the development of the MK model can be found in Banabic et al. (2021).

Stören and Rice (1975) presented an alternative theoretical approach for FLC prediction by coupling the bifurcation analysis of deformation velocity with the deformation theory. This method presents two solutions corresponding to two possibilities of neck orientation: either parallel to one of the principal strain axes or aligned along the direction of zero extension (Zhu et al., 2001). Although this model was originally proposed for isotropic material, it was then extended for anisotropic material in Li et al. (2014), coupling with perturbation analysis (Hu et al., 2018).

Recently, material deformation histories have been traceable by using optical measurement techniques. Consequently, experimental validation for the assumptions adopted in these theoretical methods can be provided. Furthermore, knowledge of material behavior before and after the necking stage is exposed. Measured results in the past demonstrated that the strain path of a material point would be changed gradually at the onset of the diffuse neck toward the plane-strain tension mode, no matter its initial forming mode (Wang et al., 2014; Vysochinskiy et al., 2016; Roatta et al., 2020). Based on the observation, Hora et al. (1996, 2013) proposed a theoretical method, named modified maximum force criterion (MMFC), by taking into account the transition of strain path beyond the diffuse neck. This method was further extended to consider the effects of different phenomena on the derived FLC, such as temperature and strain-induced martensite transformation (Krauer et al., 2007), curvature and thickness (Hora and Tong, 2006), and distortional hardening (Manopulo et al., 2015), post-necking behavior (Pham et al., 2018). In addition, Paraianu et al. (2010) suggested adding two parameters to the MMFC model to improve its predictability, which was validated for DC01 steel sheets. Pham et al. (2019a) investigated the MMFC formulation under a special case of constitutive equations based on a power hardening law with the von Mises yield function. Lian et al. (2018) successfully implemented the MMFC using a non-associated flow rule. Zajkani and Bandizaki (2017) corporate the MMFC with vertex model to determine the diffuse and localized necks.

The summaries reveal that these theoretical models provide good predictions for the FLC of some particular materials. However, no existing model can be applied to any metallic sheets (Abed-Meraim et al., 2014; Banabic et al., 2020). Each one has its own advantages and limitations. The MMFC model is attractive currently because it provides the prediction of strain path evolution, which is able to be validated experimentally. A previous comparative study (Pham et al., 2021b) pointed out that the MMFC provides excellent predictions for the right side of FLC of a large set of aluminum and steel sheets. However, this model exhibits restrictions in practical use. Aretz (2004) reported a singularity issue of this model when it is employed with a yield criterion with plane facets. Pham et al. (2018) pointed out that its prediction for the forming limit at the plane-strain mode (FLC_0) is strongly sensitive to the selection of hardening law. Moreover, the theoretical assumption of plane-strain state behaved as a sufficient condition of forming limits in this model is considered "too strong" even unrealistic, as discussed later on.

This study presents a new criterion (MMFC2) for predicting the FLC of sheet metal based on the MMFC. Details on the formulation, as well as the numerical implementation of the MMFC, are revisited. The reliability of theoretical assumptions requested in MMFC is discussed. Based on these discussions, a new equation for governing the strain path change beyond the diffuse neck is introduced. Moreover, a new criterion for detecting strain localization under plane-stress conditions is proposed. The performance of the proposed criterion is compared with that of the original MMFC in predicting the FLC of three automotive sheet metals. The related data that are needed to predict their FLC were published in the Benchmark of Numisheet 2014 conference. The use of three different hardening laws and three yield functions is examined in the analogy. Experimental validation of MMFC2 predictions for FLC of CR4 mild steel sheets is provided. In addition, a comparison between the performance of MMFC2 and MK model is presented.

2. Modified maximum force criterion

2.1. Formulation

There is a well-established assumption for ductile sheet metals that the state of the material's deformation gradually changes toward the plane-strain tension at the onset of the diffuse neck. The reality of the assumption has been discussed early by Sowerby and Duncan (1971) even under an unchanged loading condition. Nowadays, the history of deformations can be traced, for example, using the digital image correlation (DIC) method. That is a validation for the assumption of strain path change after the diffuse neck.

Based on the observation, Hora et al. (1996) introduced MMFC, a theoretical approach to estimating the FLC of sheet metals, in the form

$$\frac{\partial \sigma_1}{\partial \varepsilon_1} + \frac{\partial \sigma_1}{\partial \beta} \frac{\partial \beta}{\partial \varepsilon_1} \geq \sigma_1. \tag{1}$$

Here, σ_1 is the major Cauchy stress; $\beta = d\varepsilon_2/d\varepsilon_1$ is the ratio of principal strain increments; ε_1 and ε_2 are the major and minor principal strains, respectively. In the stages of homogeneous deformation, β is a constant depended on the forming mode, and the second term in the left-hand side of Eq. (1) vanished. The equation is simplified to the maximum force criterion, proposed by Swift (1952). As soon as the diffuse neck initiation, the deformation is inhomogeneous, and the strain path change is taken into account. Rearranging the equation leads to the evolution

$$\frac{\partial \beta}{\partial \varepsilon_1} = \frac{\sigma_1 - \frac{\partial \sigma_1}{\partial \varepsilon_1}}{\frac{\partial \sigma_1}{\partial \beta}} \tag{2}$$

The equality condition in Eq. (2) indicates an assumption proposed by Hora et al. (2013) that the strain path should change to keep the force unchanged until the localized neck is formulated. The sufficient condition for localized neck occurrence is assumed that the forming mode reaches the plane-strain tension. In other words, the forming limit is reached as soon as

$$\beta = 0 \tag{3}$$

That means Eq. (1) is a necessary condition rather than a criterion for necking detection. Eq. (3) is the sufficient condition for determining the forming limits.

2.2. Implementation

2.2.1. Isotropic hardening

Under the associated flow rule, both yield and potential surfaces can be described by a convex function $F(\boldsymbol{\sigma}, \bar{\varepsilon}) = \bar{\sigma}(\boldsymbol{\sigma}) - H(\bar{\varepsilon}) \leq 0$, where $\bar{\sigma}(\boldsymbol{\sigma})$ and $H(\bar{\varepsilon})$ are the equivalent and reference stresses of the current stress state. Here, $\alpha = \sigma_2/\sigma_1$ is the stress ratio. Hence, $\bar{\sigma}(\boldsymbol{\sigma}) = \bar{\sigma}(\sigma_{11}, \sigma_{22}, \sigma_{12}) = \sigma_1 \bar{\sigma}(1, \alpha)$ since the shear component, σ_{12} is omitted for FLC calculation.

The equivalent plastic strain increment, $d\bar{\varepsilon}$ can be defined as the plastic multiplier of the corresponding stress state, for example

$$d\bar{\varepsilon} = d\lambda, \text{ and } d\varepsilon_{1,2} = d\lambda \frac{\partial F}{\partial \sigma_{1,2}} \tag{4}$$

Numerical implementation of MMFC requires two auxiliary functions $f(\alpha) = \bar{\sigma}/\sigma_1 = \bar{\sigma}(1,\alpha)$ and $g(\beta) = \Delta\bar{\varepsilon}/\Delta\varepsilon_1$ to describe relationships between the equivalent parts and the first principal components. It is worth noticing that $f(\alpha)$ here is the reciprocal of the one presented in Hora et al. (2013).

For a given yield function, the strain increment ratio can be calculated as

$$\beta = \frac{d\varepsilon_2}{d\varepsilon_1} = \frac{\partial F/\partial \sigma_2}{\partial F/\partial \sigma_1} = \frac{\partial \bar{\sigma}/\partial \sigma_2}{\partial \bar{\sigma}/\partial \sigma_1} \tag{5}$$

Theory of equivalent plastic work states

$$dW = \bar{\sigma}d\bar{\varepsilon} = \sigma_1 d\varepsilon_1 + \sigma_2 d\varepsilon_2 \tag{6}$$

Hence, an explicit expression of $g(\beta)$ is achieved, for example

$$g(\beta) = \frac{1 + \alpha\beta}{f(\alpha)} \tag{7}$$

Therefore, the terms $\partial \sigma_1/\partial \varepsilon_1$ and $\partial \sigma_1/\partial \beta$ of Eq. (2) can be calculated as follows

$$\frac{\partial \sigma_1}{\partial \varepsilon_1} = \frac{\partial \sigma_1}{\partial \bar{\sigma}} \frac{\partial \bar{\sigma}}{\partial \bar{\varepsilon}} \frac{\partial \bar{\varepsilon}}{\partial \varepsilon_1} = g(\beta)H'/f(\alpha), \tag{8}$$

$$\frac{\partial \sigma_1}{\partial \beta} = \frac{\partial \sigma_1}{\partial \alpha} \frac{\partial \alpha}{\partial \beta} = -\bar{\sigma}\frac{f'(\alpha)}{[f(\alpha)]^2} \frac{\partial \alpha}{\partial \beta} = -H\frac{f'(\alpha)}{[f(\alpha)]^2}/\beta'(\alpha). \tag{9}$$

In these equations, $H = H(\bar{\varepsilon})$ for short explanation denotes the hardening law, and the operator $(')$ denotes the first derivative of the function. Noted that the yield condition, i.e. $\bar{\sigma}(\sigma) = H(\bar{\varepsilon})$ is adopted in Eq. (8). Substituting these equations into Eq. (2) yields

$$\frac{\partial \beta}{\partial \varepsilon_1} = \left(g(\beta)\frac{H'(\bar{\varepsilon})}{H(\bar{\varepsilon})} - 1 \right) \frac{f(\alpha)}{f'(\alpha)} \beta'(\alpha) \tag{10}$$

Eq. (10) is used to update β iteratively until the condition expressed in Eq. (3) is reached.

2.2.2. Distortional hardening

Experimental results of several materials (Pham et al., 2019b; Lee et al., 2019) exhibit the distortion of yield surface during plastic deformation. For such materials, the value of $f(\alpha)$ is dependent on the value of the equivalent plastic strain as well. Thus, the aforementioned implementation of MMFC can be cumbersome. Manopulo et al. (2015) introduced an alternative method for implementing MMFC by using first and second derivatives of $\bar{\sigma}(\sigma)$. The implementation method can take the distortional hardening behavior into account. In this method, the luxury function $f(\alpha)$ can be evaluated as

$$f(\alpha) = \frac{d\bar{\sigma}}{d\sigma_1} = \frac{\partial \bar{\sigma}}{\partial \sigma} \frac{\partial \sigma}{\partial \sigma_1} + \frac{\partial \bar{\sigma}}{\partial \sigma} \frac{\partial \sigma}{\partial \sigma_2} \frac{\partial \sigma_2}{\partial \sigma_1} = q : \left(\frac{\partial \sigma}{\partial \sigma_1} + \alpha \frac{\partial \sigma}{\partial \sigma_2} \right) \tag{11}$$

where $q = \frac{\partial \bar{\sigma}}{\partial \sigma}$ is the normal vector of yield locus. While the strain increment ratio can be calculated as

$$\beta = \frac{\partial \bar{\sigma}/\partial \sigma_2}{\partial \bar{\sigma}/\partial \sigma_1} = \left(q : \frac{\partial \sigma}{\partial \sigma_2} \right) \left(q : \frac{\partial \sigma}{\partial \sigma_1} \right)^{-1} \tag{12}$$

Their derivatives can be calculated as

$$f'(\alpha) = \frac{\partial f}{\partial \sigma} : \frac{\partial \sigma}{\partial \alpha} \tag{13}$$

$$\beta'(\alpha) = \frac{\partial \beta}{\partial \sigma} : \frac{\partial \sigma}{\partial \alpha} \tag{14}$$

where

$$\frac{\partial f}{\partial \sigma} = \frac{1}{\sigma_1} \left(q - f\frac{\partial \sigma_1}{\partial \sigma} \right) \tag{15}$$

$$\frac{\partial \sigma}{\partial \alpha} = \sigma_1 \left(\frac{\partial \sigma}{\partial \sigma_2} - \frac{1}{\alpha} \frac{\partial \sigma}{\partial \sigma_1} \right) \tag{16}$$

$$\frac{\partial \beta}{\partial \sigma} = \left(q : \frac{\partial \sigma}{\partial \sigma_1} \right)^{-1} \left[\frac{\partial q}{\partial \sigma} : \left(\frac{\partial \sigma}{\partial \sigma_2} - \beta \frac{\partial \sigma}{\partial \sigma_1} \right) \right] \tag{17}$$

Substituting Eqs. (11)–(17) into Eq. (10) derives the increment of β in the post-necking region. The expression is interpreted with the equivalent stress and its derivatives, which allowed the use of a distortional yield function, as discussed in Manopulo et al. (2015).

3. New criterion for localized neck prediction

This section proposes a new criterion, the so-called MMFC2, for FLC prediction. The motivation of the proposed criterion is hinged on the strain path change beyond the diffuse neck, which was originally discussed in the MMFC by Hora and co-workers (Hora et al., 1996, 2013). Additionally, an implementation scheme for the new criterion is detailed with the use of an isotropic hardening law.

3.1. Proposal of MMFC2

The originality of MMFC rests on the reality of these assumptions made in Eqs. (2) and (3), no matter how it was implemented numerically. With a given forming mode, these assumptions relate to the necessary and sufficient conditions for determining the forming limit or strain localization. The reliability of these conditions is revisited and discussed. Based on these discussions, new criteria for governing the strain path change and detecting the initiation localization are suggested.

3.1.1. Strain path evolution

As discussed before, Eq. (2) requests an unchanged force acting on the material's cross-section from the initiation of the diffuse neck to the formation of the localized neck. However, the assumption is rarely true, even though in the case of the uniaxial tensile test. In such a case, the loading force estimated at the instance of a localized neck may be less than that of the uniform elongation. As discussed in Manopulo et al. (2015), Pham et al. (2021c), Pham and Kim (2022), the difference may be up to 10% for many steel and aluminum sheets. It is suggested that Eq. (2) enforces a faster changing-rate $\partial\beta/\partial\varepsilon_1$ than the reality. Experimental validation of this changing rate is difficult even with DIC due to inevitable noises contained in the measured data. Moreover, the noises blow up the data, which is calculated by the ratio of small quantities, like β in this study. Fortunately, simulation results achieved from a finite element analysis (FEA) can help to understand the behavior in detail.

For this purpose, a finite element (FE) model is developed in Abaqus/Explicit version 2020 to simulate a uniaxial tensile test of the DP780 sheet. The reasons for selecting this material are twofold. At first, this material was investigated in the previous study of the authors (Pham et al., 2021c). As so, the material model can be used directly without calibration. Secondly, this material exhibits weak anisotropy (Ha et al., 2013), which allows using the von Mises yield function in the plasticity description to reduce the computational time. In the FE model, solid elements C3D8R are adopted to model the one-eight of the specimen due to the symmetry. Details on boundary conditions applied in these simulations can be found elsewhere (Pham et al., 2021c; Lou and Huh, 2013). In order to investigate the mesh-size effect on the simulated results, four different mesh cases are generated on the specimen. In the fine mesh case, the smallest element size is $0.1 \times 0.1 \times 0.1 \ mm^3$, which is small enough to capture the material behavior under necking conditions. Fig. 1 presents details on these mesh cases.

Fig. 2 shows the contour comparison of the equivalent plastic strain distribution on the simulated tensile specimens, whereas, Fig. 3 compares their force predictions. The comparisons reveal the sensitivity of the simulated results on the adopted mesh size. Decreasing the element size refines the strain localization observed in the center area and presents a lower prediction for the loading force after the maximum.
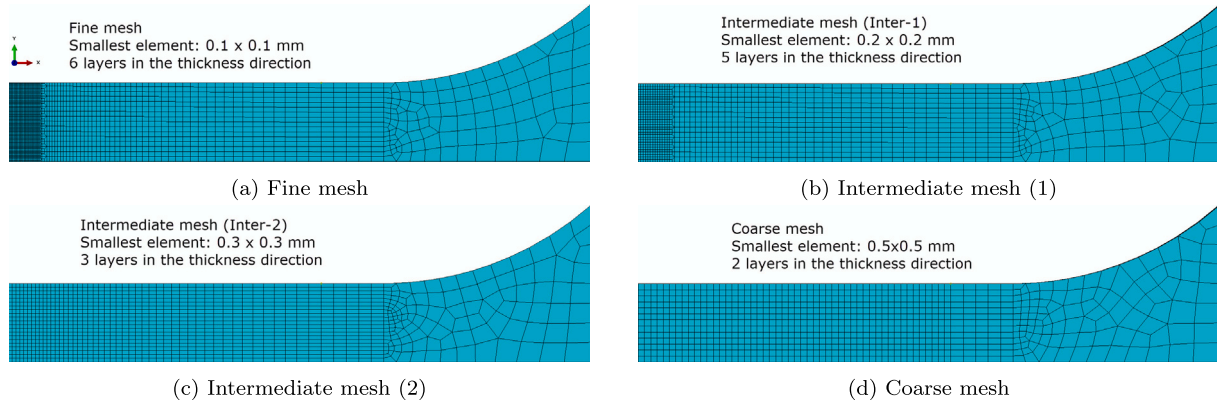
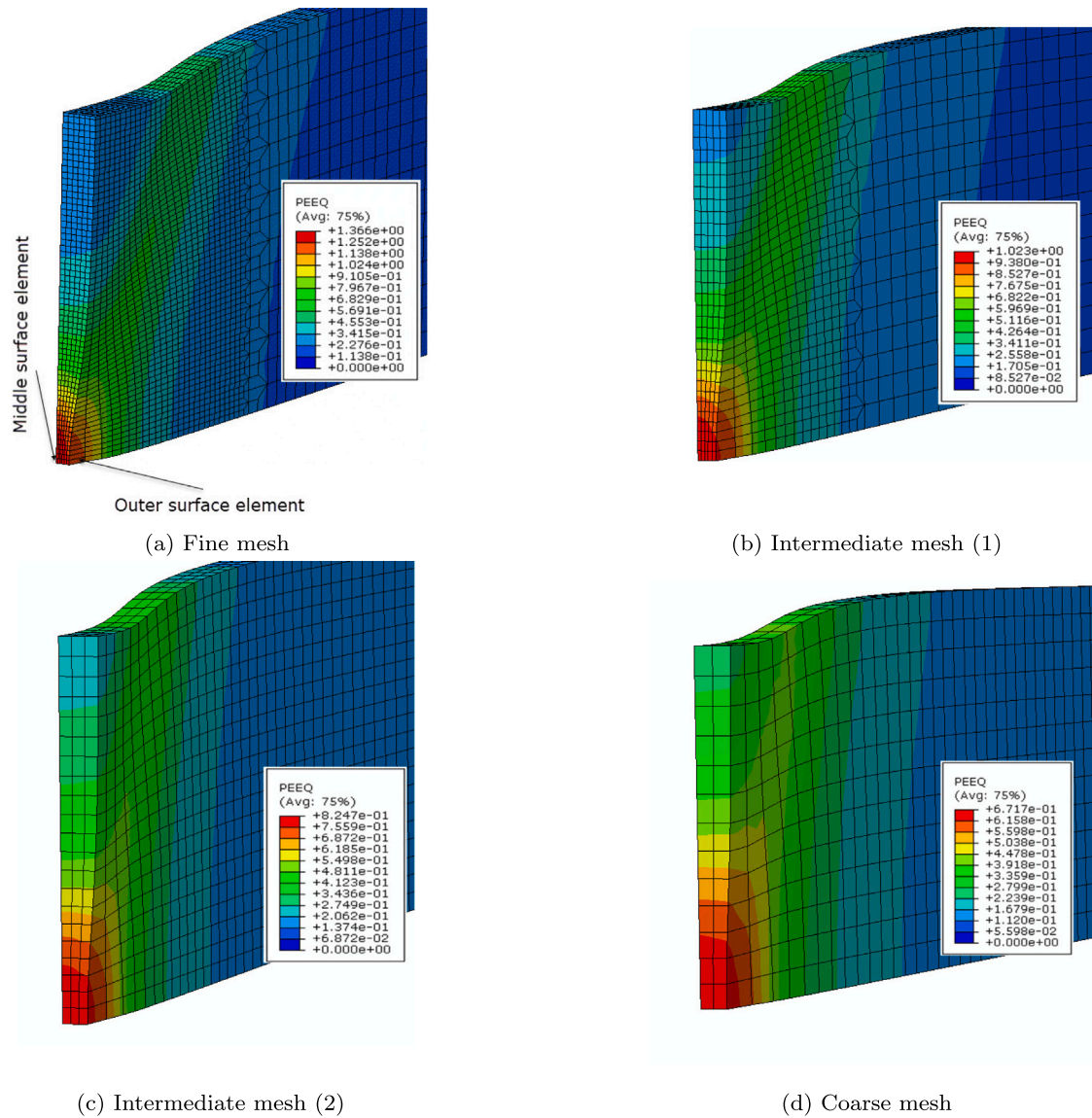**Fig. 1.** Four mesh cases used in simulations of the uniaxial tensile test of DP780 sheet.

Fig. 2. Mesh size effect on the equivalent plastic strain distribution of the simulated DP780 tensile specimens.

Moreover, the same material model is adopted into the MMFC code developed in Pham et al. (2018) to predict the necking strain of the

DP780 sheet under the uniaxial tension. Fig. 4 shows a comparison between the predictions of the β evolution of the center elements located
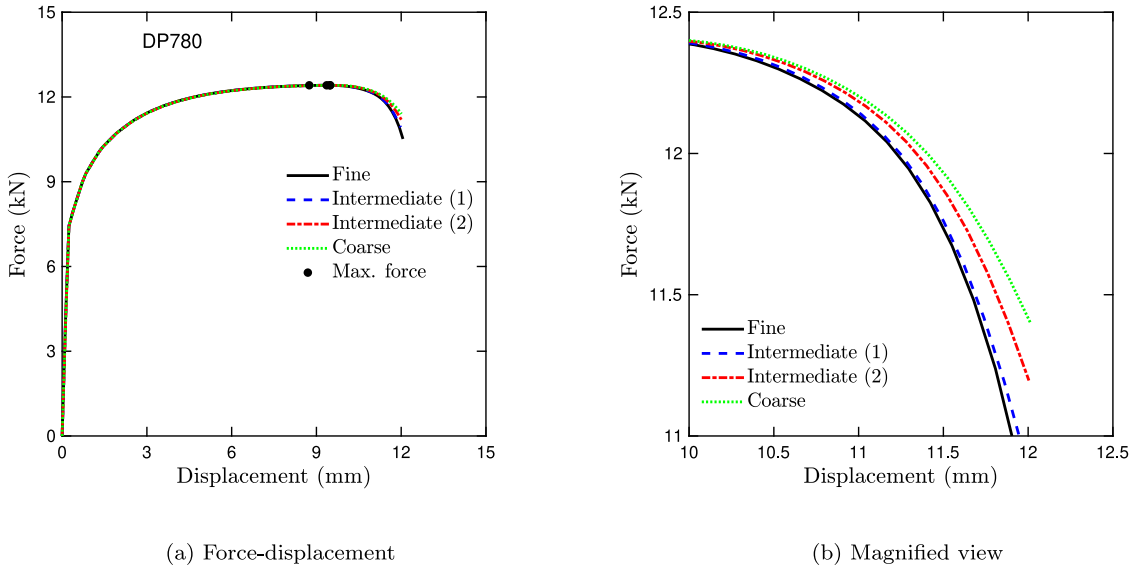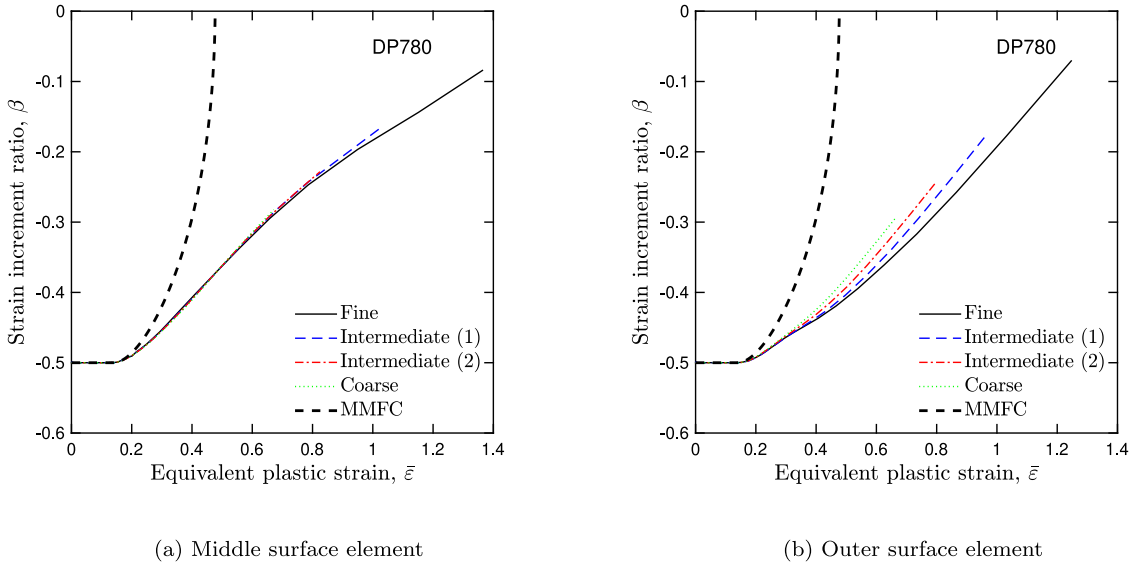
(a) Force-displacement

(b) Magnified view

Fig. 3. Comparison of force predictions of four mesh cases.

(a) Middle surface element

(b) Outer surface element

Fig. 4. Comparison between β evolution predicted by MMFC and FE simulations for DP780 sheet.

at either the specimen's outer or middle surfaces. In this figure, the value of β estimated at the ith step is approximated via the maximum and middle principal plastic strain components (denoted by ε_{1p} and ε_{2p}) as follows

$$\beta^i = \frac{\varepsilon_{2p}^i - \varepsilon_{2p}^{i-1}}{\varepsilon_{1p}^i - \varepsilon_{1p}^{i-1}} \qquad (18)$$

In addition, the β evolution estimated based on the MMFC code is also plotted in this figure for comparison. As seen in this figure, the mesh size presents a significant effect on the β evolution observed in the element located at the outer surface of the specimen. However, the effect is negligible in the element located on the middle surface. Furthermore, the evolution evaluated by MMFC is remarkably faster than that of FE simulations, either for the outer or middle elements.

The difference is believed to be due to the coarse assumption made by Eq. (10) that requests an unchanged loading force from the diffuse neck to the localized neck. Back to Fig. 3, the mesh size has no effect on the force prediction before the maximum. However, after the maximum force, the higher force is predicted as the larger element size

is employed. The observation is consistent with the result of β change presented in Fig. 4b, whereas the faster β change is observed as the larger mesh is used. The β evolution derived in MMFC is considered as the boundary of the FEA results, which may be achieved when an infinite element size is imposed.

To refine the assumption and make it closer to reality, a scaling factor, ξ, is suggested to update β as follows

$$\Delta\beta = \xi \left(g(\beta) \frac{H'(\bar{\varepsilon})}{H(\bar{\varepsilon})} - 1 \right) \frac{f(\alpha)}{f'(\alpha)} \beta'(\alpha) \Delta\varepsilon_1. \qquad (19)$$

As a result, this factor controls the changing rate of β beyond the diffuse neck. If $\xi = 1$, the procedure secures the original scheme proposed by Hora et al. (2013). When $\xi < 1$, the factor slows down the β change and postpones the strain localization.

Fig. 5a compares the β evolution estimated by several scaling factors with that derived from the middle-surface element of the FEA with the fine mesh. For a more detailed comparison, Fig. 5b presents the slope of $\beta - \bar{\varepsilon}$ curves.

As seen in these figures, the higher value of the scaling factor is imposed, the faster evolution of β is achieved. With $\xi = 0.5$, the
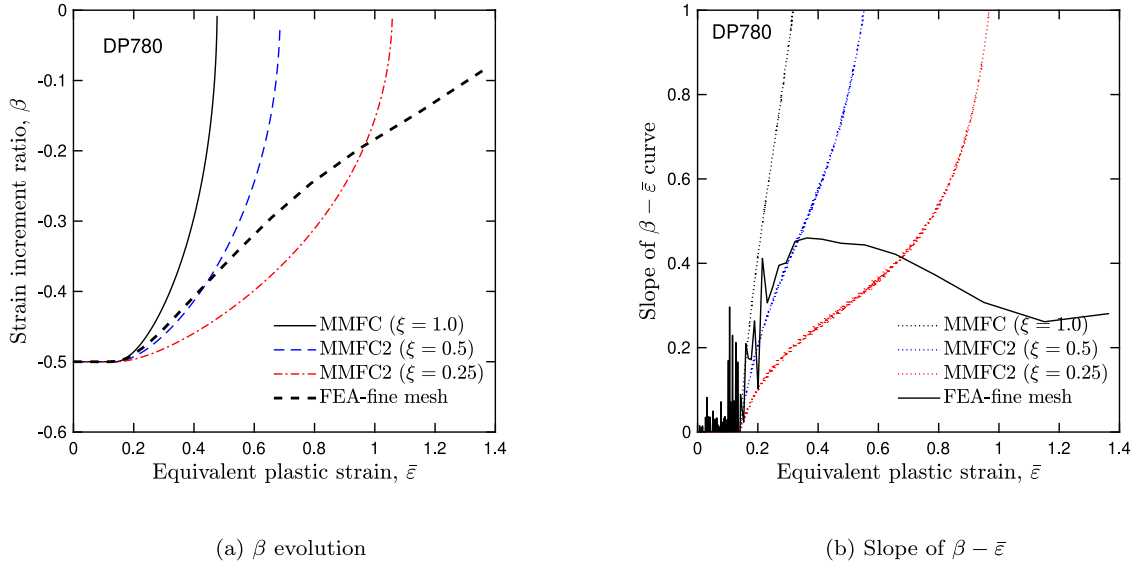
(a) β evolution

(b) Slope of $\beta - \bar{\varepsilon}$

Fig. 5. Effect of the scaling factor on the prediction of β evolution.

(a) Strain histories of necking points

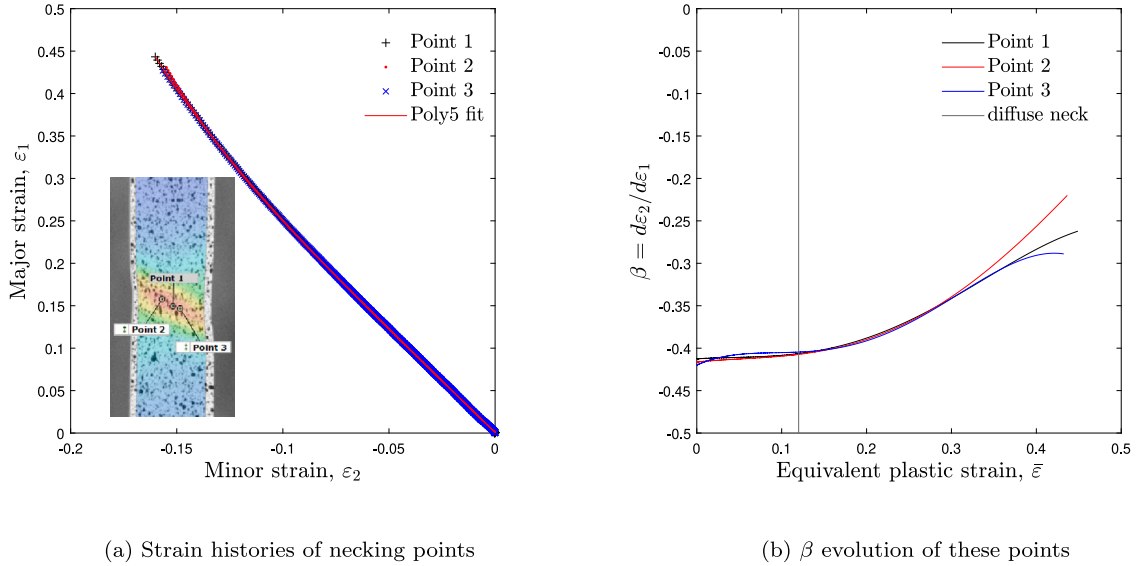(b) β evolution of these points

Fig. 6. Experimental observation of strain path change in uniaxial tension of DP780 sheet.

calculated β evolution agreed well with the FEA prediction, up to a value of $\bar{\varepsilon} = 0.5$. Afterward, the FEA simulated β is extremely smaller than the calculated one based on the MMFC2.

Despite many numerical noises contained in the early stage of the calculated slope of the FEA result, a prediction with $\xi = 0.5$ is preserved in the FEA curve. Remarkably, the deviation is started at $\bar{\varepsilon} = 0.3$. Thus, it is suggested that ξ should be a function of $\bar{\varepsilon}$ to capture the evolution of β in the entire range of $\bar{\varepsilon}$ presented in Fig. 5. However, $\xi = 0.5$ would be a good enough approximation for the neck detection purpose.

3.1.2. Strain localization

In the original MMFC, the forming limit was determined by the condition expressed in Eq. (3). The stage of deformation at the forming limit haves to appear somewhat before the failure or fracture of the tested specimen. The forming limit is commonly represented by the initiation of the localized neck or strain localization. Therefore, the requirement of Eq. (3) in MMFC seems to be overreached and has no physical meaning.

Fig. 6a shows the strain history of several necking points observed in the uniaxial tensile test of the aforementioned DP780 sheet (Pham

et al., 2021c). In order to track the β evolution of these points, their strain histories are approximated by fifth-order polynomials, as shown in this figure. Based on these fitting functions, β can be calculated analytically and illustrated in Fig. 6b. It is worth mentioning that comparing the $\beta - \bar{\varepsilon}$ curves presented in Fig. 4 with that plotted in Fig. 6b is not straightforward. Because the simulated curves are derived with an assumption of the isotropic von Mises yield function, meanwhile, the experimental curves cover a somewhat degree of material's anisotropy.

According to this figure, β keeps almost a constant of -0.42 in the early stages of deformation, i.e., before diffuse neck. After diffuse neck or in the post-necking range, the value of β increases gradually. In other words, the forming mode of these examined material points transits gradually from the uniaxial tension (i.e., $\beta \approx -0.5$) toward the plane-strain tension (i.e., $\beta = 0$). At the last recorded stage, β has a value of 0.265, which indicates a forming mode in between these before-mentioned. Thus, the experimental forming limit should be determined at a certain deformation stage, which is prior to the plane-strain tension.

During the uniaxial tensile test, on the one hand, deformation beyond the diffuse neck is non-homogeneous leading to the β change.
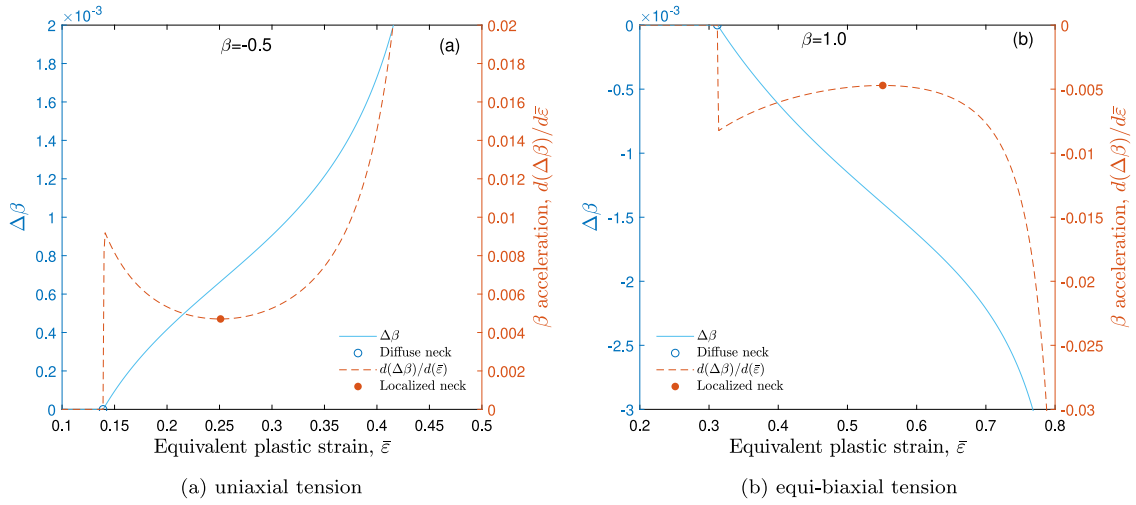
Fig. 7. Velocity and acceleration of β change predicted by MMFC for DP780 sheet observed in different forming modes.
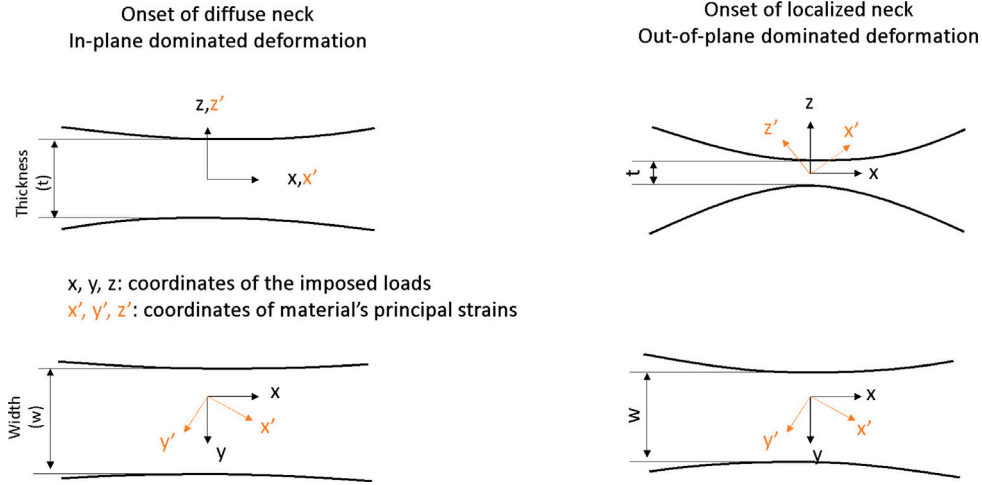

Fig. 8. Illustration of diffuse and localized necks formulated in sheet metals.

On the other hand, the deformation at the onset of strain localization is concentrated in narrow regions leading to a significant reduction in the thickness of these areas. For example, in the MK method (Banabic et al., 2021), the localization is determined by comparing the thickness strain increments of the inside necking region and its outside. However, the MMFC model is developed based on the stress and strain states of a single material point. Therefore, a new criterion is needed to detect the localization.

A β value represents a well-defined strain path under proportional loads. For instance, the uniaxial tension exposes $\beta = -0.5$ while $\beta = 1.0$ is well-known for equi-biaxial tension of an isotropic material. The amount of β increment or $\Delta\beta$ along the strain path is considered as the "velocity" of the strain path change. Fig. 7 presents the evolution of $\Delta\beta$ calculated by the original MMFC for the uniaxial and equi-biaxial tension forming modes of the DP780 sheet. It is noted that the y-axis of this figure is re-scaled to focus on the necking ranges. As seen in this figure, the velocity increases gradually and non-linearly in the post-necking range (e.g., beyond the diffuse neck). Hence, the β "acceleration" or $d(\Delta\beta)/d\bar{\varepsilon}$ is examined in this figure for comparison. At the onset of the diffuse neck, the β acceleration reaches a local minimum/maximum before an extreme diversion. The phenomenon is only observed in the results of MMFC calculation but cannot be verified in the experimental measurements. As so, reasons for the phenomenon can be explained conceptually as shown in Fig. 8.

Experimentally, non-homogeneous deformation in the post-necking range yields a rotation of the principal axes of the material point located inside the neck. Prior to the strain localization, the thickness strain is increased as gradually as before. That leads to an in-plane rotation of the principal axes, i.e., the thickness direction of the material point is assumed to be unchanged. However, after the strain localization is established, the deformation is concentrated in a narrow area, well-known as the necking band. Within this area, the out-of-plane deformation is suggested to dominate the rotation of the principal axes. That leads to a significant change in the thickness direction of the material point.

In MMFC, β regards the rotation of the principal axes of the material point. At the instance of the diffuse neck, the value of β is changed with the highest magnitude of acceleration. Thereafter, $\Delta\beta$ increases as deformation continue, as shown in Fig. 7. Nevertheless, the acceleration should decrease gently, and the $\Delta\beta$ should reach saturation, similar to the FEA result shown in Fig. 4b. However, only in-plane deformation is modeled in MMFC due to the plane-stress assumption, despite the occurrence of the out-of-plane rotation in reality. Therefore, the β acceleration is increased again to keep the equilibrium equation in MMFC and speed up the β change again. Remind that the diffuse neck in MMFC is formulated at the instance of the in-plane rotation start. Similarly, it is suggested that the strain localization is established at the moment when the out-of-plane rotation begins. Therefore, it is
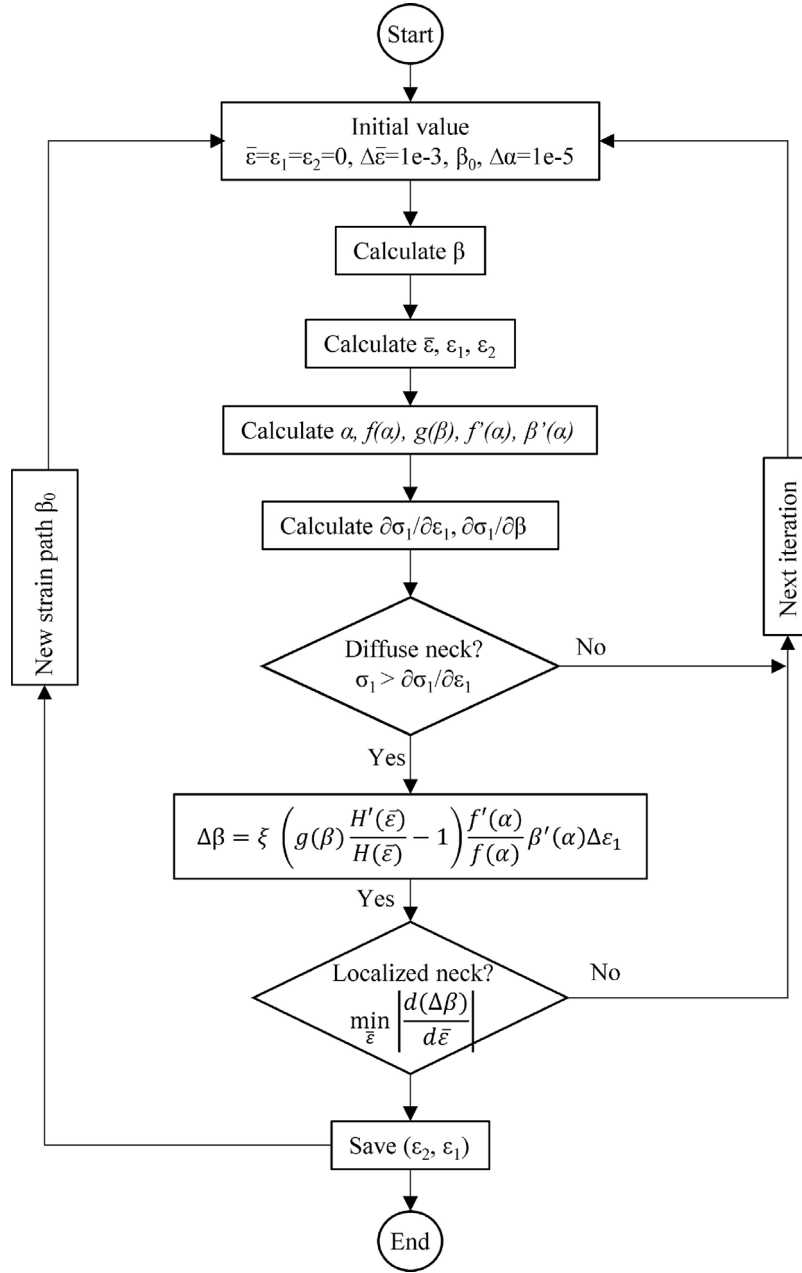
Fig. 9. Schematic diagram of the proposed MMFC2.

assumed elementally that the strain localization happens as soon as the β acceleration reaches its minimum magnitude.

Based on the discussion, the initiation of the localized neck is suggested to achieve at the moment when a local minimum/maximum of β acceleration is reached. Numerically, the criterion for detecting the localization in MMFC is proposed as follows:

$$\min_{\bar{\varepsilon}} \left| \frac{d(\Delta\beta)}{d\bar{\varepsilon}} \right| \tag{20}$$

3.2. Implementation of MMFC2

A diagram of MMFC2 implementation is depicted in Fig. 9, which is similar to the one presented in Hora et al. (2013). The procedure starts with a given forming mode, determined by a given strain increment ratio β. Noticed that the forming mode is examined in a range from the uniaxial tension to equi-biaxial tension, which results in a well-defined range $\beta \in [-0.5, 1]$. The corresponding stress ratio α is obtained

by solving the following equation numerically

$$\frac{\partial F(1,\alpha)}{\partial\sigma_2} = \beta \frac{\partial F(1,\alpha)}{\partial\sigma_1} \tag{21}$$

Subsequently, the auxiliary functions $f(\alpha)$ and $g(\beta)$ are calculated straightforwardly. The first derivative functions can be calculated using the finite difference method, such as

$$f'(\alpha) = \frac{f(\alpha + \Delta\alpha) - f(\alpha)}{\Delta\alpha} \tag{22}$$

$$\beta'(\alpha) = \frac{1}{\Delta\alpha} \left[\frac{\partial F(1, \alpha + \Delta\alpha)/\partial\sigma_2}{\partial F(1, \alpha + \Delta\alpha)/\partial\sigma_1} - \frac{\partial F(1, \alpha)/\partial\sigma_2}{\partial F(1, \alpha)/\partial\sigma_1} \right] \tag{23}$$

where $\Delta\alpha = 1E - 5$ is the finite increment of the stress ratio. The value is determined following the recommendation in Choi and Yoon (2019).

With a small increment of the equivalent plastic strain, the increments of the major and minor strains are calculated accordingly. Under the yield condition, the equivalent stress is assigned as $\bar{\sigma} = H(\bar{\varepsilon})$. Hence, the condition for the diffuse neck is checked, leading to an update of β

Table 1
Calibrated parameters of hardening laws for the tested materials.

	Swift			Voce			Pham & Kim			
	c_1 (MPa)	c_2	c_3	c_1 (MPa)	c_2 (MPa)	c_3	c_1 (MPa)	c_2 (MPa)	c_3	c_4
DP600	1097.0	0.00192	0.182	771.5	360.8	21.174	400.0	789.66	84.29	0.391
TRIP780	1503.6	0.0083	0.273	989.8	557.2	12.424	456.0	899.17	33.15	0.383
AA5182-O	615.3	0.00761	0.363	376.7	260.9	9.781	125.0	459.83	32.95	0.465

increment if necessary. Eq. (19) is used for this purpose with a constant value of ξ (e.g., $\xi = 0.5$ in this study). Again, the finite difference method is adopted to estimate the β acceleration. If the condition for localized neck expressed in Eq. (20) is satisfied, the forming limit of the current forming mode is documented. Then, the procedure is repeated for the next forming mode.

Similar to the MMFC, the implementation of MMFC2 suffers a singularity in predicting the limit strain of a perfect plane-strain forming mode where $\beta = 0$. In such a case, the strain path change does not take place. The singularity is due to the numerical errors in calculating $d\beta/d\alpha$ and can be avoided technically by excluding the case of $\beta = 0$ from the set of given forming modes. In this study, initial values of β are determined by 42 consecutive points in the range [-0.5,1]. So, the two closest points to the zero are -0.024 and 0.012, which clearly indicate the strain path change in calculation.

4. Verification with published materials

This section verifies the potential of MMFC2 with the published material data reported in the benchmark section of the Numisheet 2014 conference (Stoughton et al., 2013; Wu, 2013). This benchmark conducted experimental tests for three automotive materials, including DP600, TRIP780, and AA5182-O sheets. For each material, stress–strain data obtained from the uniaxial tensile tests conducted in seven orientations and bulge tests were provided. In addition, experimental FLCs determined from Nakajima tests were also reported for comparison.

4.1. Constitutive equations

Constitutive equations govern the material behavior under multiaxial stress states, which requires a flow rule, a hardening law, and a yield function. Since the associated flow rule is adopted in this study, several hardening laws and yield functions are examined. A hardening law reproduces the relation between the equivalent plastic strain and the reference stress. Within the published experimental data for each tested material, the benchmarking committee recommended several hardening laws with their calibrated parameters. Among them, Swift and Voce models, which were widely used in automotive sheet metal forming simulations, are adopted in this section to cope with the demand. In addition, the application of a new hardening law proposed in Pham and Kim (2017) is examined in this study. Formulations of these hardening laws are expressed as follows:

Swift: $H(\bar{\varepsilon}) = c_1(c_2 + \bar{\varepsilon})^{c_3}$ (24)

Voce: $H(\bar{\varepsilon}) = c_1 - c_2 \exp(-c_3\bar{\varepsilon})$ (25)

Pham & Kim: $H(\bar{\varepsilon}) = c_1 + c_2(1 - \exp(-c_3\bar{\varepsilon})).(\bar{\varepsilon} + 0.002)^{c_4}$ (26)

where $c_1 \sim c_4$ are parameters of these functions. These parameters were calibrated in the previous work (Pham et al., 2021a) and be reported in Table 1.

For each tested material, stress–strain data and Lankford coefficients obtained from uniaxial tensile tests in each 15° from the rolling direction were covered by the benchmarking committee. In addition, equi-biaxial stress–strain data were derived from bulge tests. Due to the anisotropy of the tested materials, three yield criteria including

Table 2
Calibrated parameters of yield functions for the tested materials.

	Hill48				Yld2k		
	DP600	TRIP780	AL5182-O		DP600	TRIP780	AL5182-O
h_1	0.5514	0.5761	0.5202	α_1	1.0546	1.0097	0.9416
h_2	0.5423	0.5282	0.5459	α_2	0.9400	0.9407	1.0329
h_3	0.4486	0.4239	0.4798	α_3	0.9899	1.0660	1.0611
h_4	1.5951	1.4889	1.6548	α_4	1.0059	1.0069	1.0320
				α_5	1.0325	1.0425	1.0230
				α_6	1.1837	1.1327	1.0220
				α_7	1.0697	1.0098	1.0229
				α_8	0.9427	0.9713	1.0992
				m	6	6	8

von Mises (labeled by "Mises"), Hill's quadratic (Hill, 1948) (labeled by "Hill48"), and Yld2000-2d (Barlat et al., 2003) (labeled by "Yld2k") are adopted to describe their yield surface. The equivalent stress defined in these functions is given under the plane stress condition as follows

von Mises: $\bar{\sigma} = \sqrt{\sigma_{11}^2 + \sigma_{22}^2 - \sigma_{11}\sigma_{22} + 3\sigma_{12}^2}$ (27)

Hill48: $\bar{\sigma} = \sqrt{h_1\sigma_{11}^2 + h_2\sigma_{22}^2 + h_3(\sigma_{11} - \sigma_{22})^2 + 2h_4\sigma_{12}^2}$ (28)

Yld2k: $\bar{\sigma} = \left\{ \frac{1}{2} \left[|X_1' - X_2'|^m + |2X_1'' - X_2''|^m + |2X_2'' - X_1''|^m \right] \right\}^{1/m}$ (29)

where $h_1 \sim h_4$ are parameters of the Hill48 function; m is the exponent coefficient and $X_{1,2}'$ and $X_{1,2}''$ are the principal values of the two stress linear transformations of the Yld2k function. In total, Yld2k function requires the exponent m and eight anisotropic parameters $\alpha_1 \sim \alpha_8$ (see Barlat et al. (2003)). The detail in the calibration of these parameters was discussed in the previous works (Pham et al., 2018, 2021a) and is not repeated here. Table 2 presents the calibrated parameters for each examined material. The derived yield functions and hardening laws are employed to calculate the FLC for the tested materials based on the original MMFC and proposed MMFC2. The predicted results are compared to the measured data reported from the benchmark.

Fig. 10 compares the measured data on the yield locus of the tested materials with the predictions based on the three mentioned yield functions. In addition, their predictions for the relationship between the stress ratio, α, and the strain increment ratio, β, are also plotted in this figure. For a comprehensive comparison of these material's models, their predictions of normalized yield stress and Lankford coefficient are presented in Appendix. According to Fig. 10, von Mises and Hill48 functions present similar yield loci for each material. However, the results derived from the Yld2k functions show a more flattened shape than the others, especially in the plane-strain regions. The differences in the yield loci predictions lead to significant differences in the estimated $\beta - \alpha$ curves. Similar to the yield loci prediction, the Hill48 functions provide similar curves to the one of the von Mises. However, the results of the Yld2k function appear with dissimilar shapes that contain a mostly linear line observed in the plane-strain region (i.e., $\alpha \sim 0.5$). The linear lines in the predicted $\beta - \alpha$ curves of the Yld2k functions may lead to singular predictions of FLC, as discussed in Aretz (2007), Hora et al. (2013).
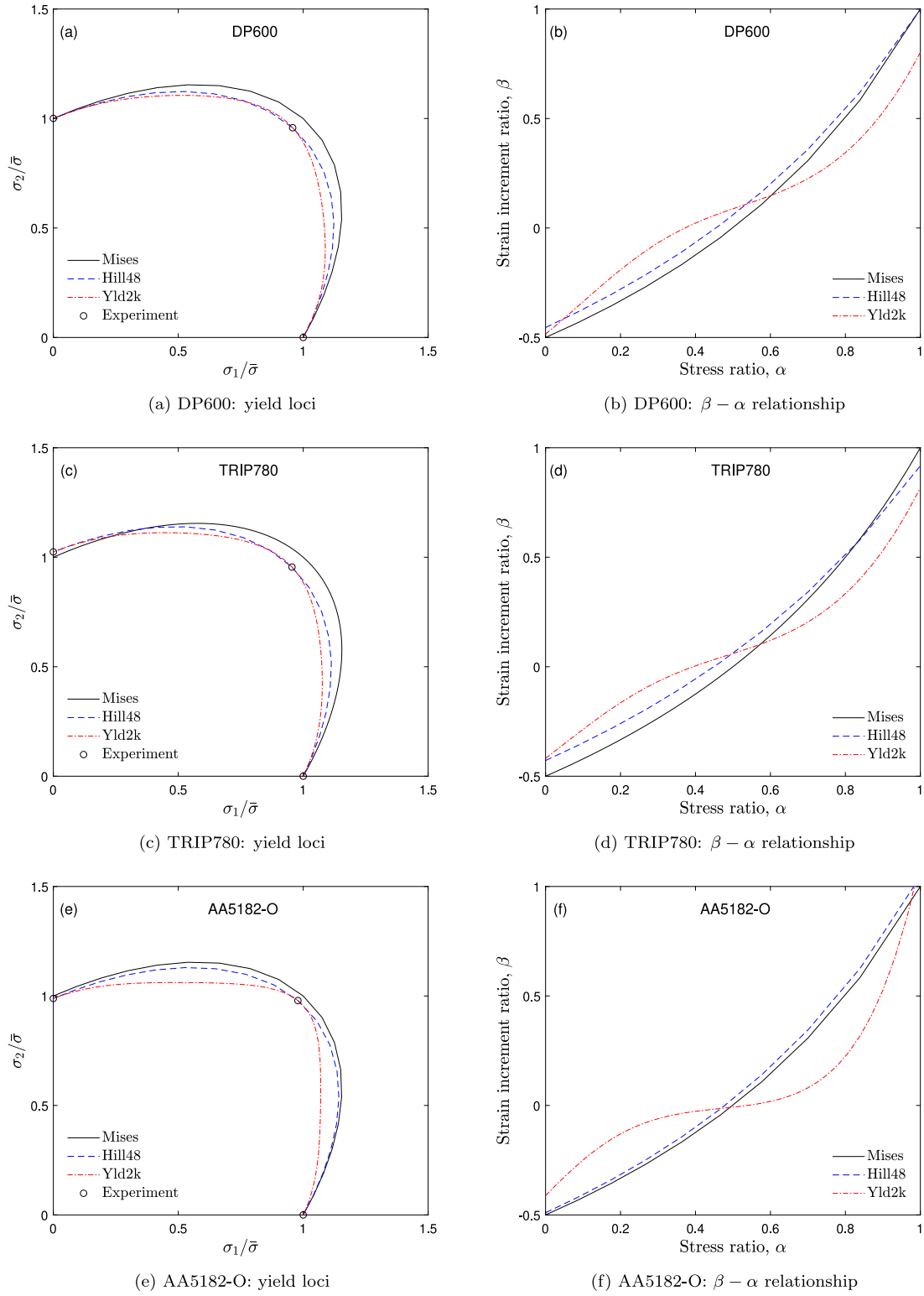
(a) DP600: yield loci

(b) DP600: $\beta - \alpha$ relationship

(c) TRIP780: yield loci

(d) TRIP780: $\beta - \alpha$ relationship

(e) AA5182-O: yield loci

(f) AA5182-O: $\beta - \alpha$ relationship

Fig. 10. Calibrated yield loci and their corresponding predictions of $\beta - \alpha$ relationship of the tested materials.

4.2. Comparison

Figs. 11–13 show comparison results of FLC predictions for DP600, TRIP780, and AA5182-O sheets, respectively, based on differences in constitutive equations as well as the calculation frameworks. Within the same constitutive model, MMFC and MMFC2 provide the same prediction for the forming limit at the plane-strain region for each examined material.

For all tested materials, the MMFC2 presents lower predicted FLCs than that of MMFC when the von Mises and Hill48 yield functions are adopted. Compared to the experimental data, the MMFC2 improves the predictions by these yield functions, obviously.

However, the performance of the Yld2k yield function does not improve in the current implementation of the MMFC2. Compared to the predictions of MMFC, the MMFC2 lowers down the left side of FLCs but higher up the right side of two steel materials. Especially, MMFC2
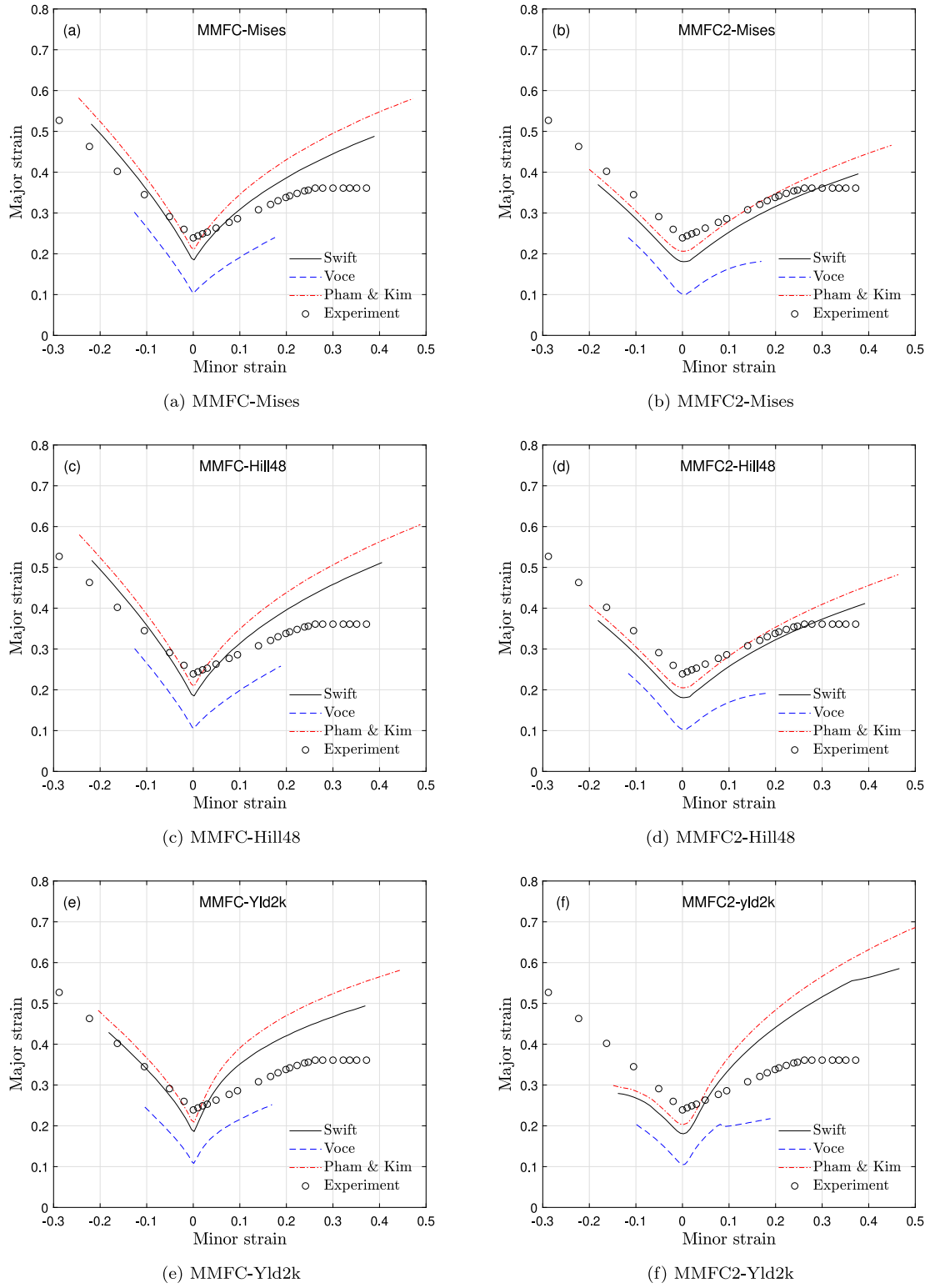
(a) MMFC-Mises

(b) MMFC2-Mises

(c) MMFC-Hill48

(d) MMFC2-Hill48

(e) MMFC-Yld2k

(f) MMFC2-Yld2k

Fig. 11. FLC prediction of DP600 sheets based on different criteria.

presents a singularity in the FLC prediction of AA5182-O material, whereas the singularity is not observed in the forecast of MMFC. It is suggested that the MMFC2 is more sensitive to the adopted yield function than the MMFC. Therefore, a proper material model should be used in MMFC2 to predict sheet metal's FLC.

Nowadays, the Yld2k yield function is widely used in sheet metal forming simulations due to its excellent ability to capture material's anisotropy by means of either normalized yield stress or Lankford coefficient. In this manner, this model outperforms the von Mises and Hill48 yield functions. The advantage of the Yld2k criterion is owing to its formula, which takes the shear stress component, σ_{12}, into account with two parameters. However, the shear stress component is totally ignored in the computational framework of MMFC and MMFC2. In these approaches, the yield loci and $\beta - \alpha$ relationship formulated with the principal stresses are the most important characteristics of a selected yield function. In this manner, excluding the shear stress
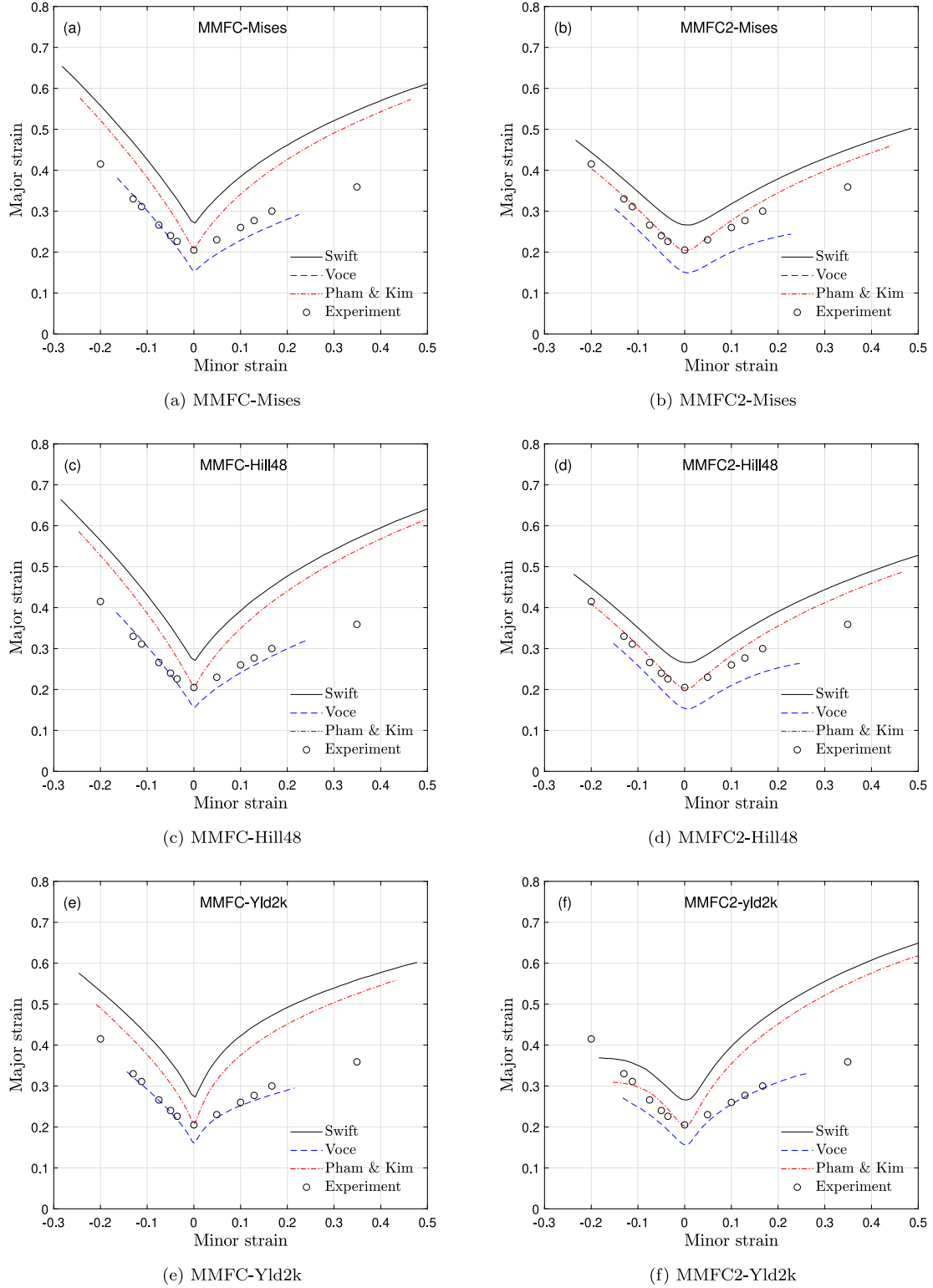
Fig. 12. FLC prediction of TRIP780 sheets based on different criteria.

in the Yld2k yield function presents flatter $\beta - \alpha$ curves than one of either von Mises or Hill48 yield functions, as shown in Fig. 10. That raises unexpected errors in calculating the $\beta'(\alpha)$ numerically, even the singularity as discussed in Aretz (2007), Hora et al. (2013). Thus, using Yld2k in conjunction with either MMFC or MMFC2 frameworks is recommended for materials that show a more "curvature" $\beta - \alpha$ curve.

It is not recommended to use this yield function for materials that show a "flattened" curve.

The comparison demonstrates the potential of the proposed MMFC2 approach, especially when it is used with von Mises and Hill48 yield functions. Further validation is needed to evaluate the performance of the proposed MMFC2.
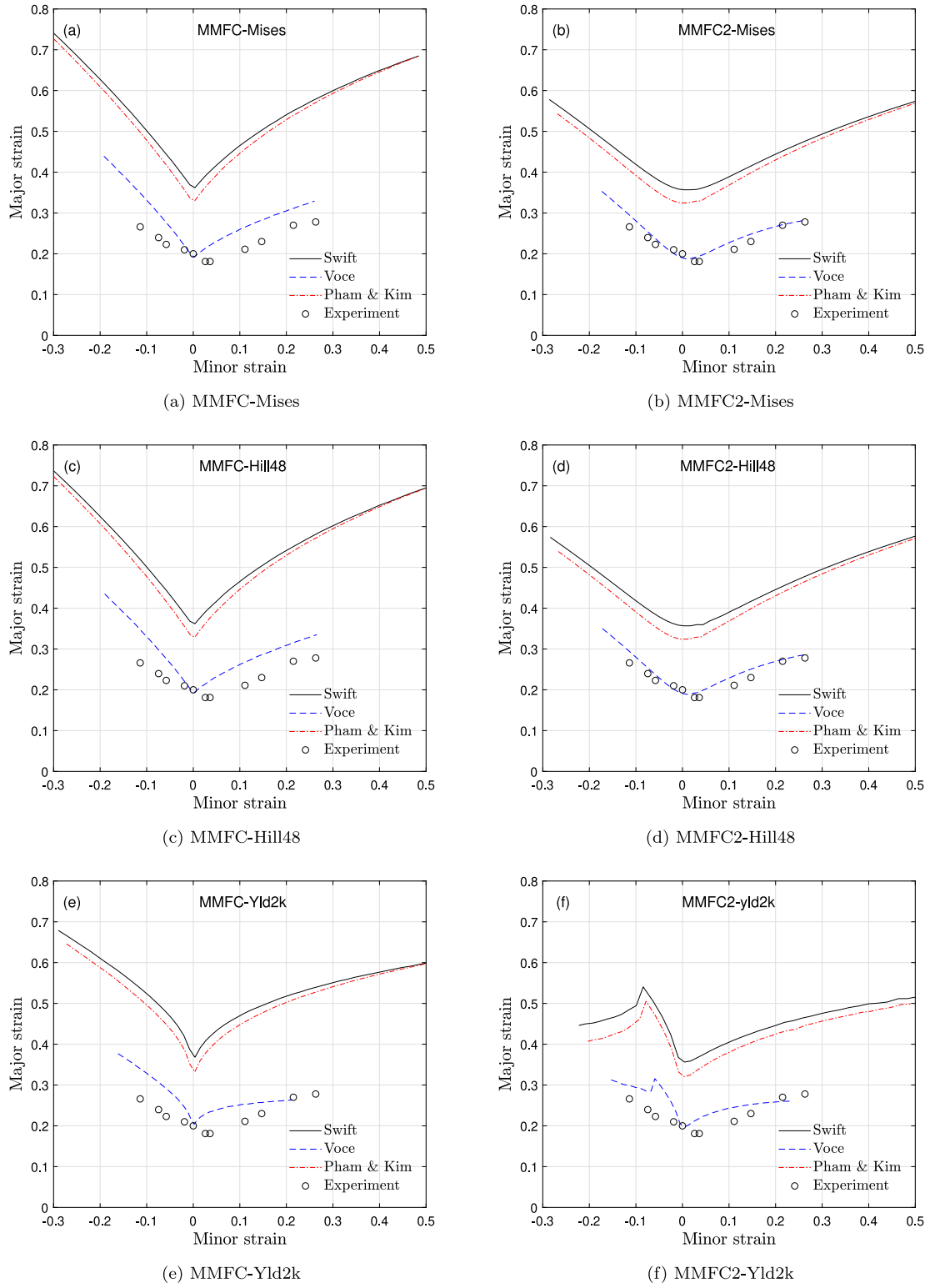
Fig. 13. FLC prediction of AA5182-O sheets based on different criteria.

4.3. Effect of the scaling factor ξ

Recall the results of the von Mises yield function and Swift hardening law shown in Figs. 11b for DP600 sheets, the prediction was obtained with a scaling factor of $\xi = 0.5$. The calculation process with several values of ξ is repeated, and the achieved results are plotted in Fig. 14 to clarify its effect on the calculated FLC based on MMFC2. As seen in this figure, the level of FLC is strongly dependent

on the imposed scaling factor, except for the FLC_0. The higher value of the scaling factor is employed, the lower FLC is derived. The same observation is expected with other constitutive models.

The scaling factor regards the rotation rate of the principal axes of the considered material point. Since the left and right sides of an FLC represent different forming processes, i.e., deep drawing and pure stretching, respectively, different scaling factors can be applied in calculating the corresponding forming limits, as suggested empirically
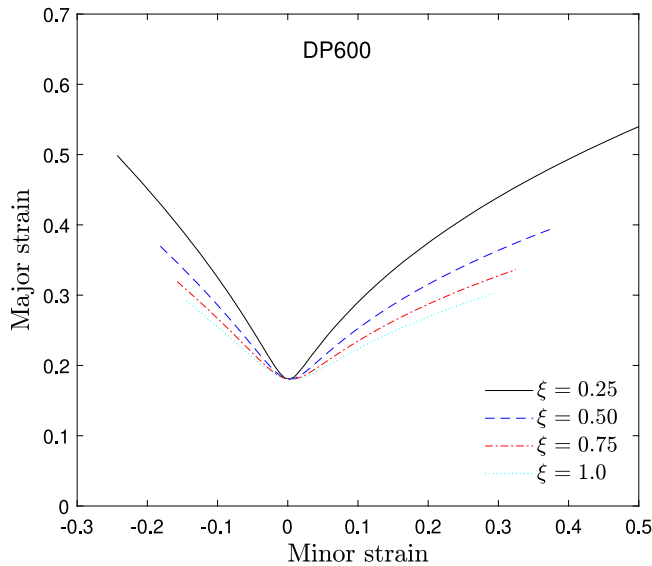
Fig. 14. Sensitivity of the scaling factor on the predicted FLC of DP600 sheets based on MMFC2.

Table 3
Material properties obtained from uniaxial tests of CR4 sheets.

Orientation	RD	DD	TD
Young modulus (GPa)	190	193	191
Yield stress (MPa)	154.8	154.0	150.8
Ultimate tensile strength (MPa)	295.4	298.2	290.3
Maximum uniform deformation	0.239	0.247	0.241
Elongation (%)	54.7	49.6	52.5
Lankford coefficient	2.1	1.876	2.577

Table 4
Inputs and calibrated parameters of hardening law and yield functions for CR4 sheets.

Input	k_0	k_{45}	k_{90}	k_b	R_0	R_{45}	R_{90}	R_b	
	1.0	1.037	1.015	1.278	2.1	1.876	2.577	1.054	
Hill48	h_1	h_2	h_3	h_4					
	0.3208	0.6792	0.2915	1.5537					
Yld2k	α_1	α_2	α_3	α_4	α_5	α_6	α_7	α_8	m
	1.0115	1.0540	0.6823	0.8525	0.8692	0.5654	0.9897	1.0882	6
Pham & Kim	c_1	c_2	c_3	c_4					
	155.0	420.15	55.68	0.47					

in Mu et al. (2020). However, it is preferable theoretically to adopt a constant scaling factor in calculating each side of FLC. A numerical approach, as done in Section 3.1.1, is an efficient approach to estimating the value of these scaling factors.

5. Validation

This section presents a validation of the proposed MMFC2 framework in predicting the FLC of CR4 mild steel sheets. This material is widely used in manufacturing car body parts. The thickness of the tested material is 0.9 mm.

5.1. Experiment procedure

A series of experimental tests are performed to calibrate the constitutive equations of the tested material and estimate the experimental FLC.

Uniaxial tensile tests are conducted to examine the material behavior under uniaxial tension. Following the ISO 6892-1:2009 standard, specimens are prepared in different orientations, including the rolling (RD), diagonal (DD), and transversal (TD) directions. These tests are carried out at 12 mm/min up to a strain level of 0.2% followed by 38 mm/min up to fracture. The strain evolution during these tests is captured with a 2D ARAMIS digital image correlation (DIC) system. The forces are measured by a load cell mounted on the cross-head of the testing machine. Fig. 15a presents the engineering stress–strain curves obtained from these tests. In addition, the ultimate tensile strength (UTS) determined for each specimen is also plotted in this figure. Table 3 presents the material properties of the CR4 material obtained from uniaxial tensile tests. It can be seen that the difference between these stress–strain curves is minor. Moreover, beyond the diffuse neck indicated by the UTS, the material is deformed significantly before fracture. This comparison emphasizes the importance of the post-necking behavior of the investigated material.

Additionally, a viscous bulge test is performed to characterize the material behavior under the equi-biaxial stress state. Details on the testing conditions for the bulge test were described in previous studies (Sigvant et al., 2009; Pilthammar et al., 2021) and are not repeated here. The strain evolution during the test is measured with a 3D ARAMIS DIC system. A comparison between the hardening curves obtained from the uniaxial tensile and bulge tests is provided in Fig. 15b.

As seen in this figure, the flow stresses and strains from the bulge test are significantly higher than the uniaxial tensile tests.

The experimental stress–strain data obtained from the uniaxial tensile test of the RD specimen are used as the reference or effective stress–strain relationship. Hence, the bulge stress–strain data are converted into effective data under the theory of equivalent plastic work (Sigvant et al., 2009; Pham et al., 2019b). These effective stress–strain data are used to characterize the hardening behavior of the investigated material in a wide strain range. The hardening law expressed in Eq. (26) is adopted to describe the hardening behavior. Hence, a curve fitting method, which is implemented internally in Matlab by a fit function, is employed to identify the hardening law's parameters. Fig. 16 shows the good agreement between the identified hardening law and experimental effective data.

Besides the hardening law, the yield functions expressed in Eqs. (27)–(29) are adopted to describe the yield surface of the tested material. In order to calibrate the parameters of the yield function, the stress–strain data obtained from uniaxial tensile and bulge tests are normalized by the flow stresses obtained from the uniaxial tensile test of the RD specimen. Fig. 17 shows the variation of these normalized stresses. Although the normalized stresses of the bulge test vary remarkably, the shape of the yield surface is commonly assumed to be undistorted during the FLC calculation. As so, the average values of these scatters are computed to evaluate the stress ratios, i.e., k_{45}, k_{90}, and k_b, respectively. These stress ratios, along with the Lankford coefficients, are used to determine the parameters of these functions. The inputs of the calibration procedure, as well as the calibrated parameters of these functions, are reported in Table 4. Fig. 18 compares the derived results of these yield functions with the experimental data of normalized yield stresses, Lankford values, and yield loci. In addition, the $\alpha - \beta$ relationships calculated from these functions are plotted in Fig. 18d. The comparisons reveal the anisotropies of the tested material. In such a case, the results of the von Mises function deviate significantly from the measurements, while both Hill48 and Yld2k functions capture quite well the experimental data.

Based on the ISO 12004-2 standard, a series of Nakajima tests are conducted to determine the experimental FLC of the tested material. These tests are conducted with a ram speed of 25 mm/s to reduce the effect of friction on the deformed specimens (Pilthammar et al., 2021). Within different specimen geometries, different forming modes, ranging from uniaxial to equi-biaxial tension, are observed at the center of the
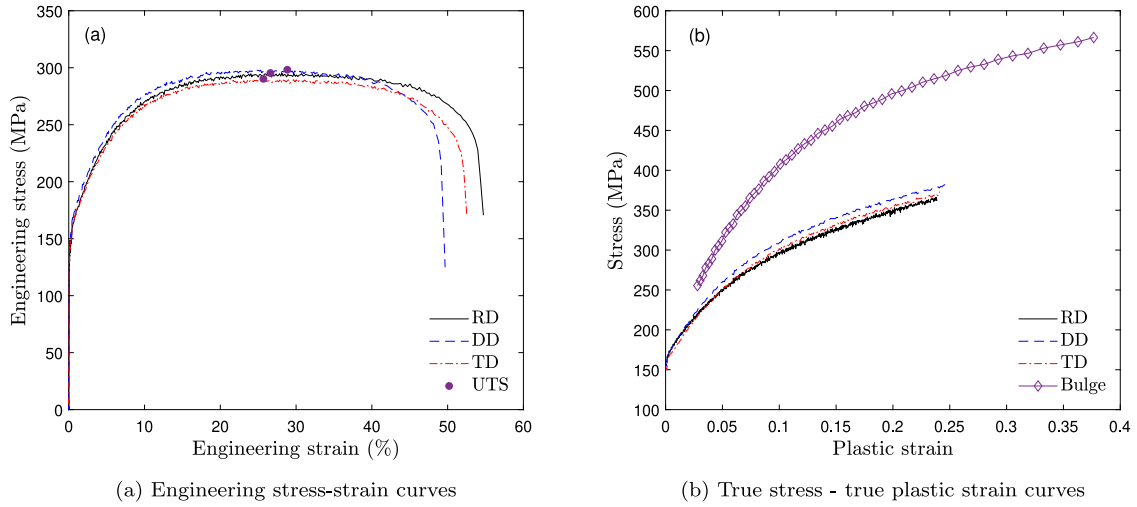
(a) Engineering stress-strain curves

(b) True stress - true plastic strain curves

Fig. 15. Hardening curves obtained from uniaxial tensile and bulge tests of CR4 mild steel sheets.
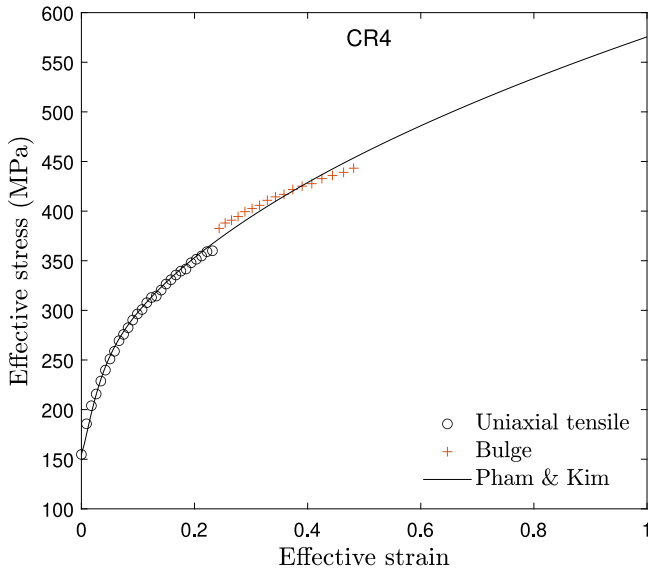

Fig. 16. Experimental data and calibrated hardening law for CR4 mild steel sheets.
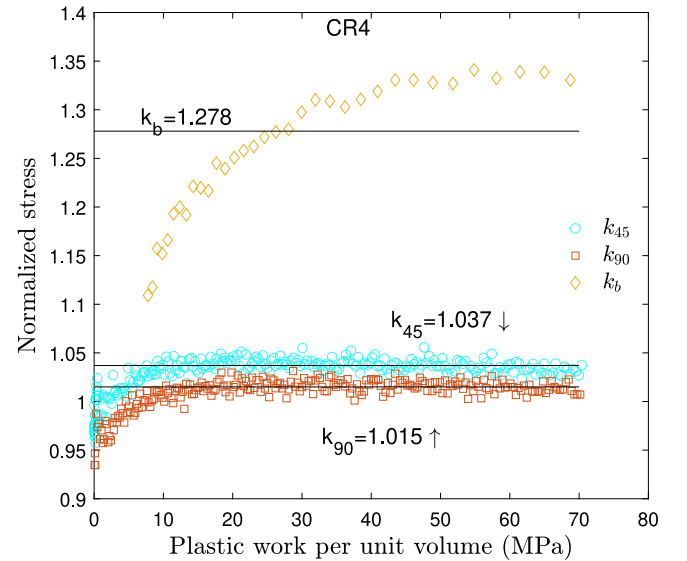

Fig. 17. Normalized yield stress of CR4 mild steel sheets.

deformed specimens. The strain history of a critical element, located on the surface of each specimen, is recorded using the 3D ARAMIS DIC system, as shown in Fig. 19. For this purpose, a camera frame rate of 60 Hz is adopted to capture the deformation. Moreover, the strain paths determined from uniaxial tensile (UT) and bulge (BT) tests are also illustrated in this figure for comparison. It is noted that texts with "W" in this figure denote the width of the corresponding Nakajima specimens.

In addition to the strain histories, the DIC measurements provide the strain rate histories of the area of interest. Sigvant et al. (2008) proposed a method to detect the necking stage of a deformed specimen using these strain rate histories. This study adopts this method to determine the limit strains of the CR4 sheets. Connecting these limit strains produces the experimental FLC of the tested material.

It is seen in Fig. 19, an abnormal strain history is observed in the case of W25 specimen. As a consequence, the necking strain of this specimen is significantly lower than that of two neighbor specimens, i.e., the UT and W50. That may be due to an unwanted event that occurred during the test. So, the necking strain of this specimen is excluded from the experimental FLC.

5.2. Formability prediction

The developed material models are employed in the framework of MMFC2 to estimate the FLC of the CR4 sheets. Although the hardening behavior of the CR4 sheet is strongly sensitive to the strain rate, the strain rate effect is not included in this model because all experimental tests were conducted at low strain rates, i.e., $\dot{\varepsilon} < 0.1$. The difference between the hardening curves identified at the quasi-static and this particular strain rate can be considered marginal, as indicated by Sigvant et al. (2019).

In order to determine the value of the scaling factor, three simulations of the uniaxial tensile test are conducted in Abaqus/Explicit package using three calibrated yield functions coupled with the identified hardening law. In these simulations, four-node reduced integration shell elements (S4R) are used to model one-quarter of the specimen using the intermediate mesh showed in Fig. 1b. Consequently, the β evolution obtained from these simulations is compared to the corresponding theoretical predictions of MMFC2 with $\xi = 0.5$, as shown in Fig. 20 for CR4 sheets. Within each yield function, the predicted β evolution agreed well with the FEA until an extreme value of equivalent plastic strain of 1.0, which is significantly larger than that of the diffuse
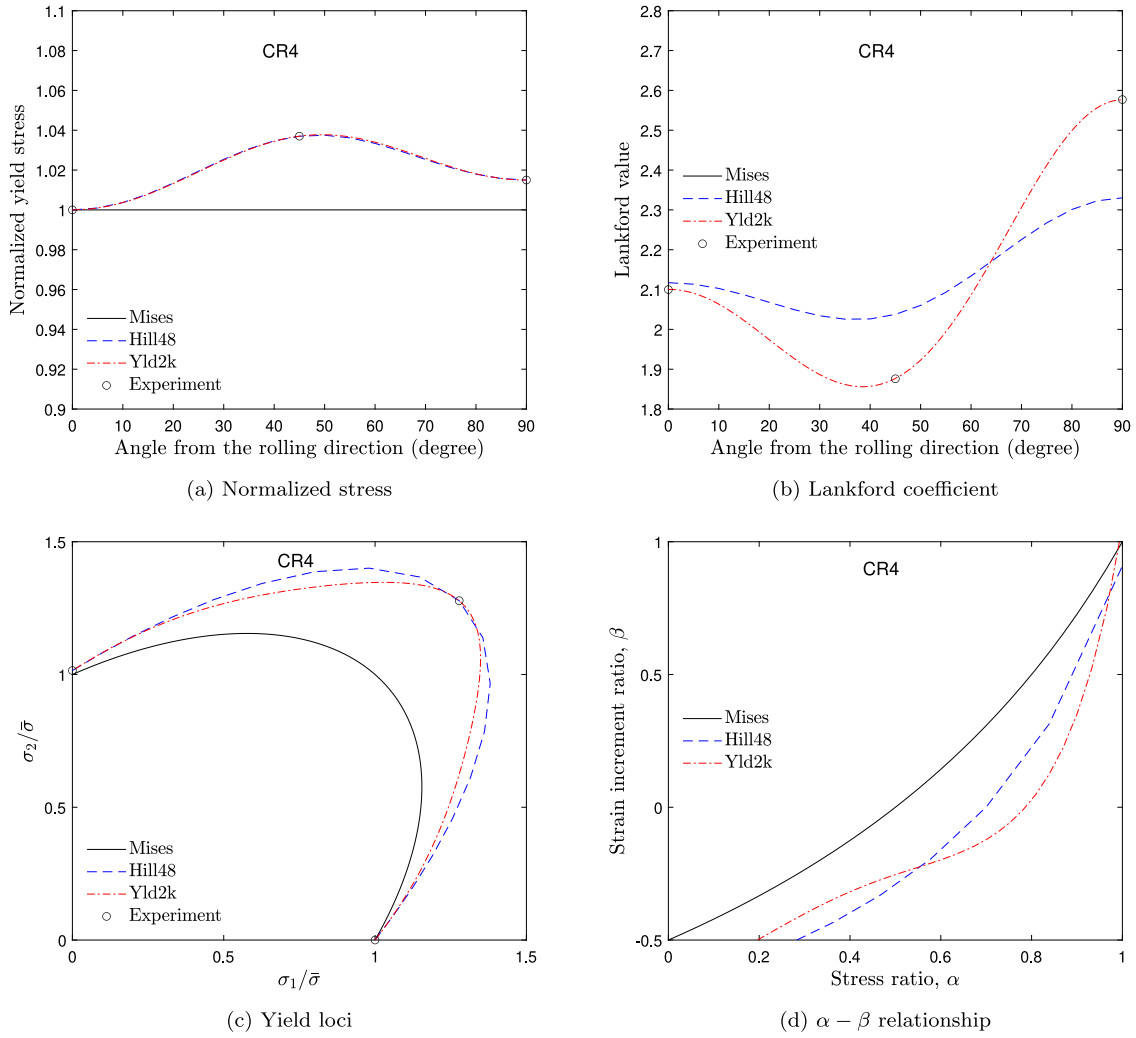
(a) Normalized stress

(b) Lankford coefficient

(c) Yield loci

(d) $\alpha - \beta$ relationship

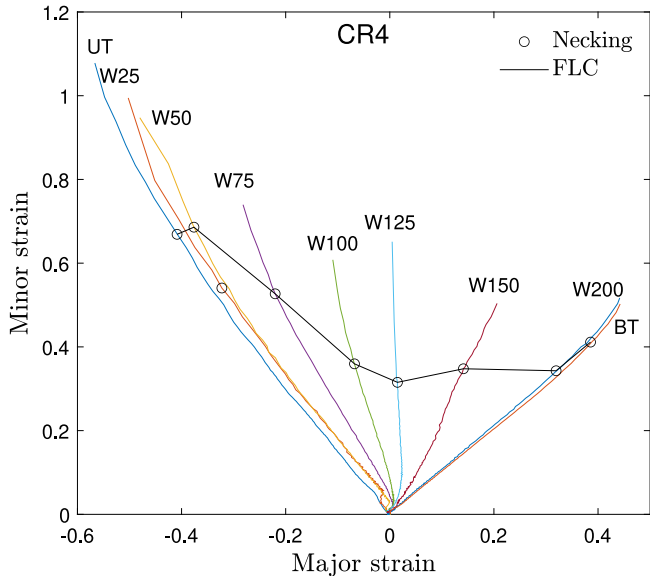**Fig. 18.** Calibrated yield functions of CR4 mild steel sheets.

Fig. 19. Strain path evolution of deformed specimens obtained from experimental tests.

neck. Thereafter, these curves deviated from each other. Therefore, a constant scaling factor $\xi = 0.5$ is sufficient to capture the strain path change during the uniaxial tensile test of CR4 sheets. This value is adopted to predict the FLC of the tested material.

Fig. 21 shows a comparison between the predicted and measured FLC of CR4 sheets. The difference between the predicted results demonstrates the constitutive model's effect on the calculated FLC. In the plane-strain tension and surrounding regions, all of these functions slightly underestimate the measured data. In this region, Hill48 and Yld2k yield functions give similar predictions, which are a little higher than that of the von Mise function, even though their predictions for yield locus are significantly different. As discussed in Pham et al. (2018), the authors suggested that post-necking prediction of the hardening law dominates the predicted level of FLC_0. However, the selection of yield function strongly affects the estimated left and right sides of FLC, as shown in Fig. 21.

For the left side of the FLC of the CR4 sheet, the predictions of von Mises and Hill48 functions are close together and underestimate the experimental data. In contrast, their prediction for the right side of FLC is significantly higher than the measurements. The overestimation of the von Mises function is explainable by its underestimation of the equibiaxial stress, as manifested in Fig. 18c. The mismatch of the Hill48 function is believed to be due to their unsatisfying in capturing the $\beta - \alpha$ relation, focused on the range $\beta > 0$. Within this range, the Yld2k yield function presents higher estimations for α, which leads to its excellent prediction for the right side of the FLC. However, the Yld2k function
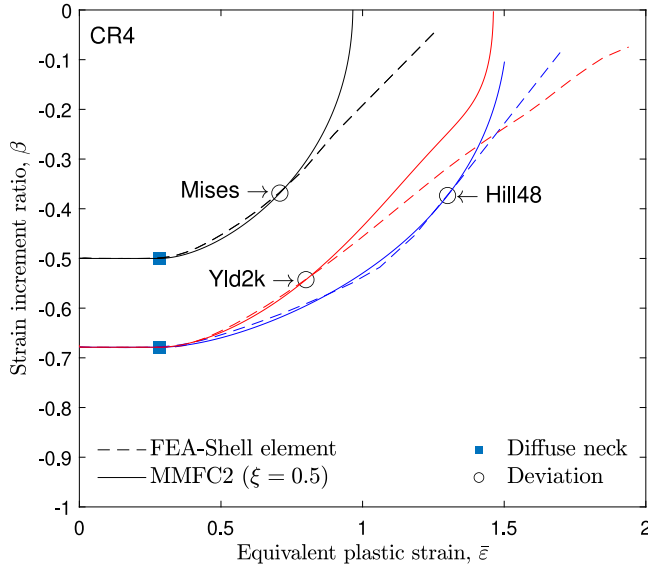
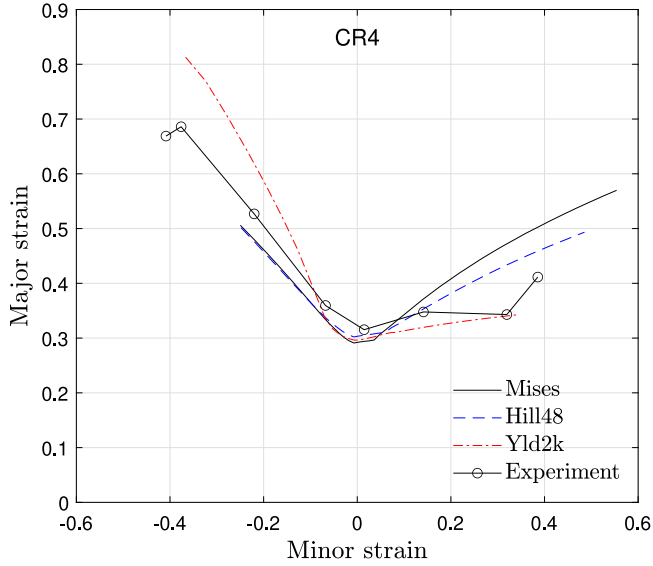Fig. 20. Determined scaling factor, $\xi = 0.5$, for CR4 mild steel sheets.

Fig. 21. Comparison between experimental FLC and the predictions of MMFC2 for CR4 mild steel sheets.
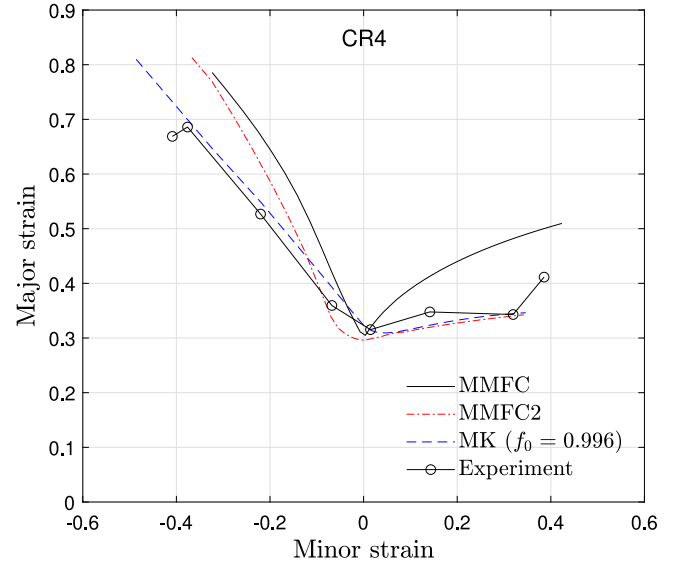

Fig. 22. Comparison of MMFC, MMFC2 and MK models for predicting the FLC of CR4 sheets.

Other models, such as MMFC2 and MK model, present mostly identical predictions for the right side of FLC, which are agreed well with the measured data of the tested material. Moreover, the MK model provides an excellent prediction for the left side of the experimental curve. The comparison highlights the advantage of the proposed MMFC2, at least again the MMFC. Furthermore, the computational time of the MMFC2 is about five times faster than that of the MK model. The advantage is more attractive when either a more complex material, such as a distortional hardening model, is adopted or a huge number of simulations is inquired, for example, in a data-driven application.

6. Discussion and conclusion

6.1. Discussion

The originality of strain path change after the diffuse neck is the significance of the MMFC. Under the plane stress condition, the second term on the left side of Eq. (1) takes the change into account. In this framework, the value of $\Delta\beta$ relates to the in-plane rotation of the principal axes of the considering material point. An additional term, which governs the out-of-plane rotation, should be considered to formulate the criterion under three-dimensional stress states. Otherwise, the shear stress component should be involved in this framework somehow to solidify its physical means. The effect of out-of-plane deformation or shear stress component on the formability of sheet metals has been investigated and discussed in several studies (Eyckens et al., 2009; Zhang et al., 2014; Mirfalah-Nasiri et al., 2016).

In the principal strain space, the forming modes regarding the FLC can be separated into deep drawing on the left side and pure stretching on the right side. Therefore, different scaling factors can be applied in calculating their limits due to their difference in the mechanism of necking initiation. Using two scaling factors may increase the flexibility of the calculation framework and provide more feasible results (Mu et al., 2020). However, the act may also increase the number of parameters to be calibrated. The scaling factor should be a function of the equivalent plastic strain $\bar{\varepsilon}$, as discussed before. Furthermore, this factor seems to be dependent on the employed constitutive models, such as yield function, hardening law (especially in the post-necking ranges), and strain rate. Without any calibration, a value of $\xi = 0.5$ is recommended for sheet metals. The reliability of this recommendation for use with an anisotropic yield function was validated for CR4 sheets.

overestimates the measurement on the left side. The observation is related to the $\beta - \alpha$ estimation in the range $\beta < 0$. Particularly, the yld2k presents a lower prediction for α than the Hill48 in this range. As a result, the former predicts a higher FLC than the latter in the left branch, where the experimental measurement is in between their predictions. It may request a higher curvature yield loci to correct the misalignment, achieved with a smaller exponent parameter m of the Yld2k. The suggestion agrees well with the value of the exponent parameter $m = 4.51$, identified in the previous study for a same grade CR4 material (Pilthammar et al., 2021).

The performance of the MMFC2 with Yld2k yield function is evaluated against the computed curves based on the original MMFC and the MK model. For this purpose, the Fortran code of the MK model developed in Bandyopadhyay et al. (2019) is used in this study with a fixed value of the material imperfection, i.e., $f_0 = 0.996$. This value is adopted following the recommendation in Barlat and Richmond (2003). Fig. 22 presents a comparison of these models. As seen in this figure, the prediction of MMFC is significantly higher than the experimental data.

Comparing the deformation inside the neck with that of the outside is widely used to detect the instance of strain localization. The technique, however, may involve uncertainties of neck geometries and the pattern variations, as discussed in Martínez-Donaire et al. (2014), Roatta et al. (2020). Using an optimal event of a single variable that correlates the deformation histories of the necking regime provides the benefit of removing investigator interpretations and prejudices. Moreover, the deformation history determined by the theoretical model can be compared to the experimental tracks, which increases the reliability of the computed results. In the literature, the necking detection methods proposed by Merklein et al. (2010) and Hotz et al. (2013) consider strain acceleration as the quantifying variable. In this study, Eq. (20) is an alternative that uses the acceleration of the principal axis rotation as an indicator for neck detection.

The results of MMFC2 derived for all examined materials are promising, even though isotropic hardening laws were incorporated in these calculations. Using a kinematic hardening law coupling with a distortional yield function may improve the accuracy of numerical predictions. That would deserve further study.

6.2. Conclusion

This study details the numerical implementation of MMFC proposed by Hora et al. (1996, 2013). The strain path evolution and condition of localization were revisited in the new version of MMFC2. A scaling factor was proposed to provide a better description of the principal axes' rotation beyond the diffuse neck. Moreover, a new criterion for localized neck initiation was proposed. A detailed numerical framework of the proposed MMFC2 within these improvements was developed to calculate the FLCs of different automotive sheet metals. The following conclusions can be made after this work:

1. Performance of the original MMFC and the proposed MMFC2 is evaluated by comparing their predictions for the FLC of published materials reported in Benchmarks 1 and 2 of Numisheet 2014 conference (Stoughton et al., 2013; Wu, 2013). Using a given constitutive model, the MMFC2 presents the same prediction as the one of MMFC for the forming limits under the plane-strain tension and its surroundings. However, the former predicts lower limits than the latter for other forming modes, such as uniaxial tensions and biaxial tensions, when a quadratic yield function is adopted.

2. Comparing their predictions with different constitutive models reveal that the proposed MMFC2 is more sensitive to the imposed constitutive model than the original MMFC. Using an advanced yield function like Yld2k does not always improve the accuracy of the predictions. The reason for this drawback is due to the exclusion of the shear stress component from the calculation framework. The Yld2k yield function is recommended to use in materials that display a weak anisotropy. Care should be taken to select a proper constitutive model in predicting FLC with the proposed criterion.

3. Furthermore, the FLC predictions of MMFC2 for three published materials, i.e., DP600, TRIP780, and AA5182-O sheets, are more concordant with the experimental data than that of the original MMFC. Compared to the MMFC results, the MMFC2 improves the predictions by von Mises and Hill48 yield functions clearly. Further studies should clarify the application of the proposed MMFC2 for different automotive sheet metals.

4. Uniaxial tensile and bulge tests were conducted to calibrate several material models for CR4 mild steel sheets. Adopting these models into the MMFC2 framework yields several FLC predictions of CR4 sheets, which are compared with the experimental measurement of Nakajima tests. The prediction resulting from the Yld2k yield function coupling with Pham & Kim hardening law agreed well with the measured data. This verifies the potential of the proposed MMFC2 in predicting the FLC of sheet metals.

Declaration of competing interest

Data availability

Data will be made available on request.

Acknowledgments

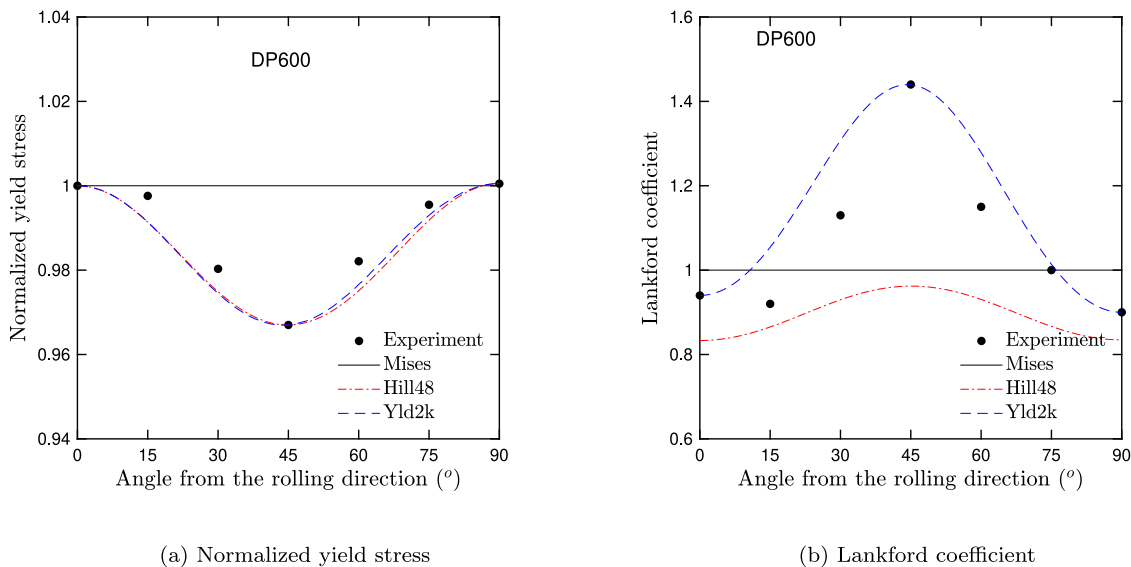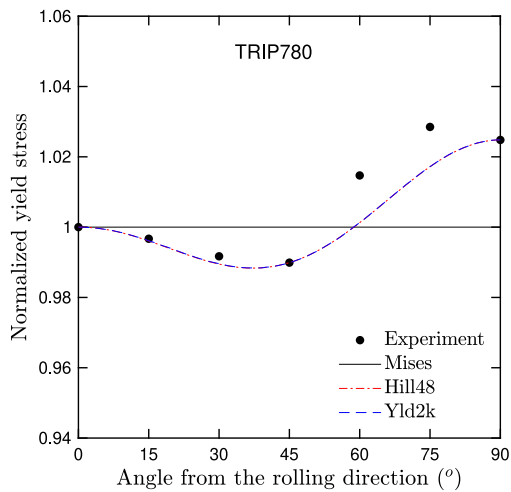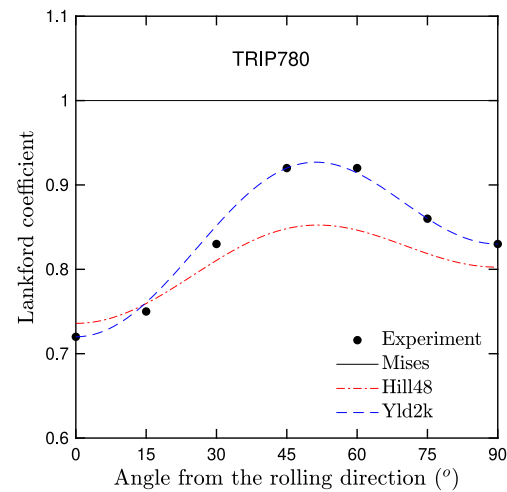(a) Normalized yield stress

(b) Lankford coefficient

Fig. A.1. Comparison of the experimental data and predicted anisotropy of DP600 sheet.
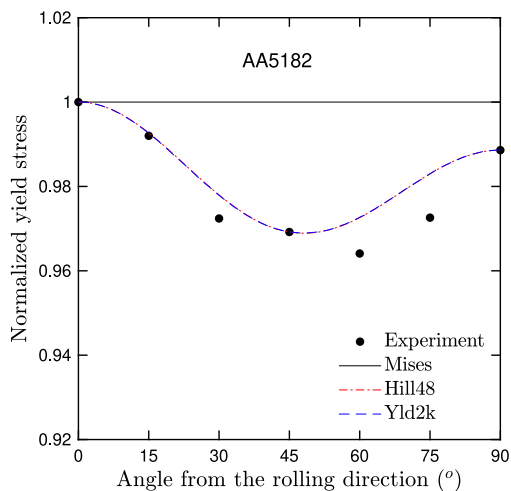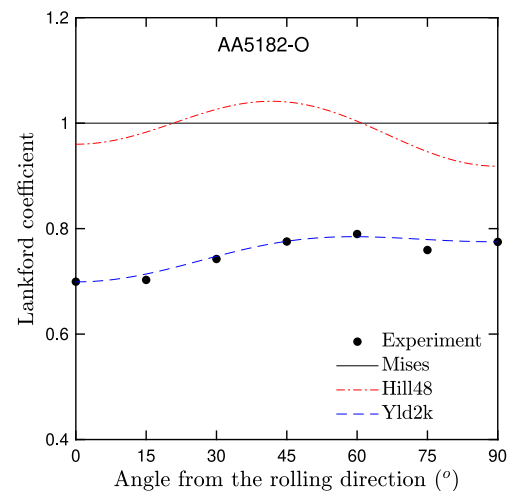
(a) Normalized yield stress

(b) Lankford coefficient

Fig. A.2. Comparison of the experimental data and predicted anisotropy of TRIP780 sheet.

(a) Normalized yield stress

(b) Lankford coefficient

Fig. A.3. Comparison of the experimental data and predicted anisotropy of AA5182-O sheet.

Appendix

This appendix presents the predictions of the three mentioned yield functions in the main text for the normalized yield stress and Lankford coefficient of three tested sheet metals (see Figs. A.1–A.3).

References

Abed-Meraim, F., Balan, T., Altmeyer, G., 2014. Investigation and comparative analysis of plastic instability criteria: application to forming limit diagrams. Int. J. Adv. Manuf. Technol. 71 (5–8), 1247–1262.

Allwood, J.M., Shouler, D.R., 2009. Generalised forming limit diagrams showing increased forming limits with non-planar stress states. Int. J. Plast. 25 (7), 1207–1230.

Aretz, H., 2004. Numerical restrictions of the modified maximum force criterion for prediction of forming limits in sheet metal forming. Modelling Simul. Mater. Sci. Eng. 12 (4), 677.

Aretz, H., 2007. Numerical analysis of diffuse and localized necking in orthotropic sheet metals. Int. J. Plast. 23 (5), 798–840.

Banabic, D., Barlat, F., Cazacu, O., Kuwabara, T., 2020. Advances in anisotropy of plastic behaviour and formability of sheet metals. Int. J. Mater. Form. 13 (5), 749–787.

Banabic, D., Kami, A., Comsa, D.-S., Eyckens, P., 2021. Developments of the Marciniak-Kuczynski model for sheet metal formability: A review. J. Mater. Process. Technol. 287, 116446.

Bandyopadhyay, K., Basak, S., Prasad, K.S., Lee, M.-G., Panda, S.K., Lee, J., 2019. Improved formability prediction by modeling evolution of anisotropy of steel sheets. Int. J. Solids Struct. 156, 263–280.

Barlat, F., Brem, J., Yoon, J.W., Chung, K., Dick, R., Lege, D., Pourboghrat, F., Choi, S.-H., Chu, E., 2003. Plane stress yield function for aluminum alloy sheets—part 1: theory. Int. J. Plast. 19 (9), 1297–1319.

Barlat, F., Richmond, O., 2003. Modelling macroscopic imperfections for the prediction of flow localization and fracture. Fatigue Fract. Eng. Mater. Struct. 26 (4), 311–321.

Bleck, W., Deng, Z., Papamantellos, K., Gusek, C.O., 1998. A comparative study of the forming-limit diagram models for sheet steels. J. Mater. Process. Technol. 83 (1–3), 223–230.

Butuc, M.C., Barlat, F., Vincze, G., 2021. The formability of twinning—Induced plasticity steels predicted on the base of Marciniak-Kuczynski theory. J. Mater Process. Technol. 287, 116496.

Butuc, M., Da Rocha, A.B., Gracio, J., Duarte, J.F., 2002. A more general model for forming limit diagrams prediction. J. Mater. Process. Technol. 125, 213–218.

Choi, H., Yoon, J.W., 2019. Stress integration-based on finite difference method and its application for anisotropic plasticity and distortional hardening under associated and non-associated flow rules. Comput. Methods Appl. Mech. Engrg. 345, 123–160.

Chu, X., Leotoing, L., Guines, D., Ragneau, E., 2014. Temperature and strain rate influence on AA5086 forming limit curves: Experimental results and discussion on the validity of the MK model. Int. J. Mech. Sci. 78, 27–34.

Djavanroodi, F., Derogar, A., 2010. Experimental and numerical evaluation of forming limit diagram for Ti6Al4V titanium and Al6061-T6 aluminum alloys sheets. Mater. Des. 31 (10), 4866–4875.

Eyckens, P., Van Bael, A., Van Houtte, P., 2009. Marciniak–Kuczynski type modelling of the effect of through-thickness shear on the forming limits of sheet metal. Int. J. Plast. 25 (12), 2249–2268.

Ganjiani, M., Assempour, A., 2007. An improved analytical approach for determination of forming limit diagrams considering the effects of yield functions. J. Mater Process. Technol. 182 (1–3), 598–607.

Ha, J., Lee, M.-G., Barlat, F., 2013. Strain hardening response and modeling of EDDQ and DP780 steel sheet under non-linear strain path. Mech. Mater. 64, 11–26.

Hill, R., 1948. A theory of the yielding and plastic flow of anisotropic metals. Proc. R. Soc. Lond. Ser. A Math. Phys. Sci. 193 (1033), 281–297.

Hill, R., 1952. On discontinuous plastic states, with special reference to localized necking in thin sheets. J. Mech. Phys. Solids 1 (1), 19–30.

Hora, P., Tong, L., 2006. Numerical prediction of FLC using the enhanced modified maximum force criterion (eMMFC). In: Numerical and Experimental Methods in Prediction of Forming Limits in Sheet Forming and Tube Hydroforming Processes. Institut für Virtuelle Produktion, ETH Zürich, pp. 31–36.

Hora, P., Tong, L., Berisha, B., 2013. Modified maximum force criterion, a model for the theoretical prediction of forming limit curves. Int. J. Mater. Form. 6 (2), 267–279.

Hora, P., Tong, L., Reissner, J., 1996. A prediction method for ductile sheet metal failure in FE-simulation. In: Proceedings of NUMISHEET. Vol. 96, pp. 252–256.

Hotz, W., Merklein, M., Kuppert, A., Friebe, H., Klein, M., 2013. Time dependent FLC determination comparison of different algorithms to detect the onset of unstable necking before fracture. In: Key Engineering Materials. Vol. 549, Trans Tech Publ, pp. 397–404.

Hu, Q., Zhang, L., Ouyang, Q., Li, X., Zhu, X., Chen, J., 2018. Prediction of forming limits for anisotropic materials with nonlinear strain paths by an instability approach. Int. J. Plast. 103, 143–167.

Hutchinson, J., Neale, K., 1978. Sheet necking-II. Time-independent behavior. In: Mechanics of Sheet Metal Forming. Springer, pp. 127–153.

Kim, Y.-S., Won, S.-Y., Na, K.-H., 2003. Effect of material damage on forming limits of voided anisotropic sheet metals. Metall. Mater. Trans. A 34 (6), 1283–1290.

Krauer, J., Hora, P., Tong, L., Berisha, B., 2007. Forming limit prediction of metastable materials with temperature and strain induced martensite transformation. In: AIP Conference Proceedings. Vol. 908, (1), AIP, pp. 1263–1268.

Kuroda, M., Tvergaard, V., 2000. Forming limit diagrams for anisotropic metal sheets with different yield criteria. Int. J. Solids Struct. 37 (37), 5037–5059.

Lee, E.-H., Choi, H., Stoughton, T.B., Yoon, J.W., 2019. Combined anisotropic and distortion hardening to describe directional response with Bauschinger effect. Int. J. Plast. 122, 73–88.

Li, S., He, J., Cedric Xia, Z., Zeng, D., Hou, B., 2014. Bifurcation analysis of forming limits for an orthotropic sheet metal. J. Manuf. Sci. Eng. 136 (5).

Lian, J., Shen, F., Jia, X., Ahn, D.-C., Chae, D.-C., Münstermann, S., Bleck, W., 2018. An evolving non-associated hill48 plasticity model accounting for anisotropic hardening and r-value evolution and its application to forming limit prediction. Int. J. Solids Struct. 151, 20–44.

Lou, Y., Huh, H., 2013. Prediction of ductile fracture for advanced high strength steel with a new criterion: Experiments and simulation. J. Mater Process. Technol. 213 (8), 1284–1302.

Manopulo, N., Hora, P., Peters, P., Gorji, M., Barlat, F., 2015. An extended modified maximum force criterion for the prediction of localized necking under non-proportional loading. Int. J. Plast. 75, 189–203.

Marciniak, Z., Kuczyński, K., 1967. Limit strains in the processes of stretch-forming sheet metal. Int. J. Mech. Sci. 9 (9), 609–620.

Martínez-Donaire, A., García-Lomas, F., Vallellano, C., 2014. New approaches to detect the onset of localised necking in sheets under through-thickness strain gradients. Mater. Des. 57, 135–145.

Merklein, M., Kuppert, A., Geiger, M., 2010. Time dependent determination of forming limit diagrams. CIRP Ann. 59 (1), 295–298.

Mirfalah-Nasiri, S., Basti, A., Hashemi, R., 2016. Forming limit curves analysis of aluminum alloy considering the through-thickness normal stress, anisotropic yield functions and strain rate. Int. J. Mech. Sci. 117, 93–101.

Mohammadi, M., Brahme, A.P., Mishra, R.K., Inal, K., 2014. Effects of post-necking hardening behavior and equivalent stress–strain curves on the accuracy of M–K based forming limit diagrams. Comput. Mater. Sci. 85, 316–323.

Mu, L., Jia, Z., Ma, Z., Shen, F., Sun, Y., Zang, Y., 2020. A theoretical prediction framework for the construction of a fracture forming limit curve accounting for fracture pattern transition. Int. J. Plast. 129, 102706.

Paraianu, L., Dragos, G., Bichis, I., Comsa, D.S., Banabic, D., 2010. A new formulation of the modified maximum force criterion (MMFC). Int. J. Mater. Form. 3 (1), 243–246.

Pham, Q.T., Kim, Y.S., 2017. Identification of the plastic deformation characteristics of AL5052-O sheet based on the non-associated flow rule. Met. Mater. Int. 23 (2), 254–263.

Pham, Q.T., Kim, Y.-S., 2022. Evaluation on flexibility of phenomenological hardening law for automotive sheet metals. Metals 12 (4), 578.

Pham, Q.T., Kim, J.J., Kim, Y.S., 2019a. Application of a graphical method on estimating forming limit curve of automotive sheet metals. Int. J. Automot. Technol..

Pham, Q.T., Lee, M.G., Kim, Y.S., 2019b. Characterization of the isotropic-distortional hardening model and its application to commercially pure titanium sheets. Int. J. Mech. Sci. 160, 90–102.

Pham, Q.T., Lee, M.G., Kim, Y.S., 2021a. New procedure for determining the strain hardening behavior of sheet metals at large strains using the curve fitting method. Mech. Mater. (ISSN: 01676636) 154, 103729. http://dx.doi.org/10.1016/j.mechmat.2020.103729.

Pham, Q.T., Lee, B.-H., Park, K.-C., Kim, Y.-S., 2018. Influence of the post-necking prediction of hardening law on the theoretical forming limit curve of aluminium sheets. Int. J. Mech. Sci. 140, 521–536.

Pham, Q.T., Mac, T.B., Kim, Y.-S., Nguyen, D.T., 2021b. A comparative investigation on theoretical models for forming limit diagram prediction of automotive sheet metals. Mech. Based Des. Struct. Mach. 1–15.

Pham, Q.T., Nguyen-Thoi, T., Ha, J., Kim, Y.-S., 2021c. Hybrid fitting-numerical method for determining strain-hardening behavior of sheet metals. Mech. Mater. 161, 104031.

Pilthammar, J., Banabic, D., Sigvant, M., 2021. BBC05 with non-integer exponent and ambiguities in Nakajima yield surface calibration. Int. J. Mater. Form. 14 (4), 577–592.

Roatta, A., Stout, M., Signorelli, J.W., 2020. Determination of the forming-limit diagram from deformations within necking instability: a digital image correlation-based approach. J. Mater. Eng. Perform. 29 (6), 4018–4031.

Schwindt, C., Schlosser, F., Bertinetti, M., Stout, M., Signorelli, J.W., 2015. Experimental and visco-plastic self-consistent evaluation of forming limit diagrams for anisotropic sheet metals: An efficient and robust implementation of the MK model. Int. J. Plast. 73, 62–99.

Sigvant, M., Mattiasson, K., Larsson, M., 2008. The definition of incipient necking and its impact on experimentally or theoretically determined forming limit curves. In: Proceedings of IDDRG'08, the International Deep Drawing Research Group, June 16-18, Olofström, Sweden, Edited By Nader Asnafi.

Sigvant, M., Mattiasson, K., Vegter, H., Thilderkvist, P., 2009. A viscous pressure bulge test for the determination of a plastic hardening curve and equibiaxial material data. Int. J. Mater. Form. 2 (4), 235–242.

Sigvant, M., Pilthammar, J., Hol, J., Wiebenga, J.H., Chezan, T., Carleer, B., van den Boogaard, T., 2019. Friction in sheet metal forming: Influence of surface roughness and strain rate on sheet metal forming simulation results. Procedia Manuf. 29, 512–519.

Son, H.S., Kim, Y.S., 2003. Prediction of forming limits for anisotropic sheets containing prolate ellipsoidal voids. Int. J. Mech. Sci. 45 (10), 1625–1643.

Sowerby, R., Duncan, J., 1971. Failure in sheet metal in biaxial tension. Int. J. Mech. Sci. 13 (3), 217–229.

Stören, S., Rice, J., 1975. Localized necking in thin sheets. J. Mech. Phys. Solids 23 (6), 421–441.

Stoughton, T.B., Shi, M.F., Huang, G., Yoon, J.W., 2013. Material characterizations for benchmark 1 and benchmark 2. In: AIP Conference Proceedings. Vol. 1567, (1), American Institute of Physics, pp. 9–14.

Swift, H., 1952. Plastic instability under plane stress. J. Mech. Phys. Solids 1 (1), 1–18.

Vysochinskiy, D., Coudert, T., Hopperstad, O.S., Lademo, O.-G., Reyes, A., 2016. Experimental detection of forming limit strains on samples with multiple local necks. J. Mater Process. Technol. 227, 216–226.

Wang, K., Carsley, J.E., He, B., Li, J., Zhang, L., 2014. Measuring forming limit strains with digital image correlation analysis. J. Mater Process. Technol. 214 (5), 1120–1130.

Wu, X., 2013. Benchmark 1-nonlinear strain path forming limit of a reverse draw: Part c: Benchmark analysis. In: AIP Conference Proceedings. Vol. 1567, (1), AIP, pp. 39–176.

Yoshida, K., Kuwabara, T., Kuroda, M., 2007. Path-dependence of the forming limit stresses in a sheet metal. Int. J. Plast. 23 (3), 361–384.

Zajkani, A., Bandizaki, A., 2017. An efficient model for diffuse to localized necking transition in rate-dependent bifurcation analysis of metallic sheets. Int. J. Mech. Sci. 133, 794–803.

Zhang, F., Chen, J., Chen, J., 2014. Effect of through-thickness normal stress on forming limits under Yld2003 yield criterion and MK model. Int. J. Mech. Sci. 89, 92–100.

Zhu, X., Weinmann, K., Chandra, A., 2001. A unified bifurcation analysis of sheet metal forming limits. J. Eng. Mater. Technol. 123 (3), 329–333.